RING ARRAY PROCESSING FOR FORWARD-LOOKING INTRAVASCULAR AND INTRACARDIAC ULTRASONIC IMAGING

COŞKUN TEKEŞ

IŞIK UNIVERSITY

2010

RING ARRAY PROCESSING FOR FORWARD-LOOKING

INTRAVASCULAR AND INTRACARDIAC ULTRASONIC IMAGING

COŞKUN TEKEŞ

B.S., Electrical Engineering, Istanbul Technical University, 1998

M.S., Electronics Engineering, Işık University, 2002

Submitted to the Graduate School of Science and Engineering
in partial fulfillment of the requirements for the degree of
Doctor of Philosophy
in
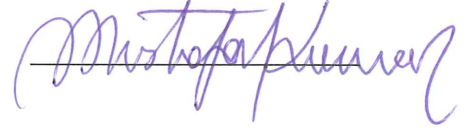Electronics Engineering

IŞIK UNIVERSITY

2010

IŞIK UNIVERSITY

GRADUATE SCHOOL OF SCIENCE AND ENGINEERING

RING ARRAY PROCESSING FOR FORWARD-LOOKING

INTRAVASCULAR AND INTRACARDIAC ULTRASONIC IMAGING

COŞKUN TEKEŞ

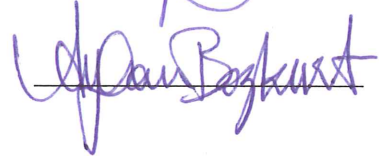
APPROVED BY:

Prof. Mustafa KARAMAN   (Işık University)

(Thesis Supervisor)

Assoc. Prof. Uluğ BAYAZIT   (İstanbul Technical University)

Assist. Prof. Ayhan BOZKURT   (Sabancı University)

Prof. Yorgo ISTEFANOPULOS   (Işık University)

Prof. Nizamettin AYDIN   (Yıldız Technical University)

APPROVAL DATE: 08/06/2010

RING ARRAY PROCESSING FOR FORWARD-LOOKING
INTRAVASCULAR AND INTRACARDIAC ULTRASONIC IMAGING

Abstract

Forward-looking (FL) catheter-based imaging systems are highly desirable for guiding interventions in IVUS and ICE applications. One of the main challenges in the array based FL-IVUS systems is the large channel count which results in increased system complexity. Synthetic phased array processing with reduced firing count simplifies the front-end and hence can enable 3-D real-time imaging. Recently, we have investigated dual-ring arrays suitable for IVUS and ICE imaging. In this dissertation, we present and explored two different optimized array designs based on dual circular and hexagonal rings that are suitable for synthetic phased array processing with reduced number of firings. We used simulated annealing to optimize the wideband PSF of the array system. The optimal firing set from different Tx-Rx elements eliminates most of the redundant spatial frequencies in the coarray and produces low side lobes and number of firings. The optimization procedure starts with the calculated wideband PSF of the full set coarray including all Tx-Rx firing combinations. In every iteration step, a predefined coarray with only one element change is compared with the previous set in terms of cost function. For the two designs, we obtained optimal reduced set by minimizing both the peak side lobe level and the integrated side lobe energy. For two test cases, we obtained reduced sets of 512 and 256 coarray elements, and constructed 2-D PSFs. The simulation results show that the optimized dual circular and hexagonal ring arrays provide up to 10-dB and 5-dB improvements, respectively, in peak near side lobe level with no widening in main lobe width. Our test results show that the side lobe levels of the dual circular and hexagonal arrays can be remarkably and controllably reduced by using simulated annealing optimization, and the resulting optimal array designs can meet the resolution and speed requirements of 3-D real time IVUS and ICE imaging.

ÖNE BAKAN DAMAR-İÇİ VE KALP-İÇİ ULTRASONİK GÖRÜNTÜLEMEDE HALKA DİZİ İŞLEME

Özet

Kanal içi ve kalp içi ultrason uygulamalarında öne bakan kateter tabanlı görüntüleme sistemleri kılavuzlu müdahale için sıklıkla istenmektedir. Öne bakan kalp içi ultrason sistemlerinin en temel zaaflarından biri sistem karmaşıklığını arttıran fazla sayıda kanal içermesidir. Yapay evreli dizi işleme tekniği kanal sayısını azaltarak ön-elektroniği basitleştirir ve böylece üç boyutlu gerçek zamanlı görüntülemeye imkan sağlar. Yakın zamanda incelediğimiz ikili halka dizi mimarisi kanal ve kalp içi görüntüleme için uygun bir yapıdır. Bu tezde, yapay evreli dizi işlemeye uygun ikili dairesel ve altıgen şeklinde iki farklı eniyilenmiş dizi yapısı keşfedilmiş ve sunulmuştur. Dizi yapısı geniş bant noktasal dağılım işlevi (NDİ) benzetilmiş tavlama yöntemiyle eniyilenmiştir. En uygun gönderme-alma (ateşleme) kümesi gereksiz mekansal frekansların büyük kısmını ortadan kaldırır ve az sayıda ateşleme ile alçak yan lob seviyesi üretir. Eniyileme yordamı tüm alıcı-verici ateşleme katışımlarının oluşturduğu tüm kümeye ait geniş bantlı NDİ oluşturularak başlar. Başlangıçta tanımlanmış eşdizi her yineleme adımında sadece bir eleman değiştirilerek bir önceki küme ile amaç maliyet (enerji) fonksiyonu cinsinden karşılaştırılır. Her iki yapı için de, hem yan lob tepe seviyesinin hem de toplam yan lob enerji seviyesinin en aza indirilmesi yöntemleriyle en uygun azaltılmış küme elde edilmiştir. Benzetimi yapılan ikili dairesel ve altıgen dizi yapıları tüm eleman kümesi olarak sırasıyla 3712 ve 1176 eleman içermektedir. Bu sayılar iki sınama durumu için 512 ve 256 elemana indirilmiş ve iki boyutlu NDİ'leri oluşturulmuştur. Benzetim sonuçları, yakın yan lob seviyesi bakımından sırasıyla 10 dB ve 5 dB iyileştirmesine rağmen ana lob eninde bir genişlemeye neden olmamıştır. Sınama sonuçlarımız ikili dairesel ve altıgen halka dizilerinde benzetilmiş tavlama eniyilenmesi kullanılmasıyla yan lob seviyesinin dikkat çekici ve kontrol edilebilir şekilde düştüğünü göstermiştir. Ve bu elde edilen en uygun dizi yapıları üç boyutlu gerçek zamanlı damar ve kalp içi görüntüleme çözünürlük ve hız gereksinimlerini karşılamaktadır.

Acknowledgement

I would like to express my sincere gratitude to my supervisor, Prof. Mustafa Karaman for giving me the opportunity to work on this subject, and for his support and patience throughout my PhD studies. Without his guidance and persistent help this dissertation would not have been possible.

I would like to thank my thesis supervising committee members Assoc. Prof. Uluğ Bayazıt and Assist. Prof. Ayhan Bozkurt, for their guidance, suggestions and very helpful comments.

I would like to gratefully and sincerely thank my doctoral dissertation committee member and dean of our faculty Prof. Yorgo Istefanopulos and chair of Electronics department Prof. Ahmet Aksen for their great support. I also thank to my other doctoral dissertation committee member Prof. Nizamettin Aydın for reading the thesis and making corrections.

I would like to particularly acknowledge and thank Prof. Levent Değertekin from Georgia Institute of Technology and his research group that directly contributed to this work by giving useful guidance and providing experimental support.

I also gratefully thank to all research assistants and faculty members of the engineering faculty.

Finally, I would like to express my wife Ayşe Tekeş and my parents for their understanding, patience, support and encouragement during the completion of my Ph. D.

Table of Contents

List of Tables

List of Figures

List of Symbols

$a(x)$	Continuous aperture function
$a_{TR}(x)$	Effective aperture function
c	Speed of sound
D	Linear dimension of an aperture
D_A	Diameter of transducer array
d	Inter-element distance
E	Energy
f	Frequency
$f(.)$	Energy (cost) function
$F(.)$	Fourier transform
$J_0(.)$	Zero-order bessel function
$J_1(.)$	First-order bessel function
$H(.)$	Point spread function to a point target
I_0	Zero-order modified bessel function of the first kind
log_{10}	Logarithm base 10
$ln(.)$	Natural logarithm
N	Number of array elements
N_d	Desired number of elements
N_f	Number of firings
$N(i)$	Neighborhood function
$n(t)$	Noise function
N_d	Desired number of firings
N_T	Number of transmit array
N_R	Number of receive array
Ps	Signal power

$p(.)$	Probability function
$P(r)$	Point spread function
$r(.)$	Received signal
Q	Number of beams
R_f	Focal depth
r	Continuous axial coordinate
R_m	Reflectivity coefficient
R	Image depth
S	Aperture surface
$s(t)$	Excitation signal
T	Temperature
T_k	Temperature in k^{th} iteration
t	Time
$U(.)$	Field Amplitude at location
$U(\theta_x, \theta_y)$	2D beam pattern
$U_{TR}(\theta)$	2-way beam pattern
x, y	Cartesian coordinates of observation plane
w	Aperture weighting coefficient
Z	Acoustic impedance
z	Depth in cartesian coordinates
$z(.)$	Linear envelope of the received signal
$z_c(.)$	Logarithmic compressed envelope of the received signal
z_f	Focal distance
α, β	Acoustic parameters of the medium
$\delta(.)$	Dirac delta function
$\Delta.$	Axial resolution
Γ	Decrementation constant
χ	Acceptance ratio
ξ, η	Cartesian coordinates of aperture plane
λ	Wavelength

$\mu(.)$	Attenuation function
ρ	Material density
$\sigma_N{}^2$	Noise variance
τ	Phase delay
θ	Angle in polar coordinates
$\theta_{3\text{-}dB}$	3-dB angular beamwidth
θ_s	Sector angle
*	1-D convolution

List of Abbreviations

ADC   Analog-to-digital converter

CMUT   Capacitive micromachined ultrasonic transducer

CSA   Conventional synthetic aperture

MRI   Magnetic resonance imaging

CT   Computed tomography

ECC   Electrical-to-mechanical coupling coefficient

EP   Electrophysiology

Fr   French

IC   Integrated circuit

ICE   Intracardiac echocardiogrpahy

IVUS   Intravascular ultrasound

LNA   Low-noise preamplifier

PV   Pulmonary veins

PVDF   Polyvinylidene fluoride

PZT   Lead zirconate titanate

SL   Side-looking

FL-IVUS   Forward-Looking IVUS

SNR   Signal to noise ratio

PSF   Point spread function

PA   Phased array

Rx   Receive

SPA   Synthetic phased array

TGC   Time-gain controlled amplifier

Tx   Transmit

Chapter 1

Introduction

1.1. Ultrasound Imaging

Ultrasound imaging has been in widespread clinical use. It is a useful way of examining many of the body's internal organs, including the heart and blood vessels, eyes, breast and abdominal organs. In many parts of the body, suspected tumors are monitored with ultrasound. It is also used to guide procedures such as needle biopsy of breast cancer. Doppler ultrasound images can help the physician see and evaluate blockages and narrowing of blood vessels. Ultrasound not only complements the more traditional diagnostic imaging technologies such as magnetic resonance imaging (MRI), computed tomography (CT), and X-ray but also enable unique and advantageous characteristics. MRI and CT have the widest range of clinical use. Both can be used to provide high quality images of different cross-sections and volumes of any part of the body. CT provides quick scan times, better imaging of bone and better resolution. The major drawback of CT is that it depends on radiation. As MRI becomes faster and cheaper, it is replacing CT for many types of examinations. MRI provides superior soft tissue contrast and is extremely flexible in terms of contrast mechanisms and functional imaging. The main drawback of MRI is that the equipments and the installation is expensive. Despite the high quality imaging with MRI and CT, the vast majority of medical diagnostic imaging is either X-ray or ultrasound.

Ultrasound refers to sound waves having a frequency above the human ear's audibility limit of about 20 KHz. The advantages of ultrasound as imaging modality are numerous. With up to a 100 frames per second, ultrasound can capture the dynamic movement of organs and details of blood flow in real time. Its relatively low cost and non-ionizing radiation makes it more attractive than other imaging

modalities of similar capabilities. The portability of ultrasound machines makes it possible to use them outside of the radiology and cardiology departments [1].

A commercial state-of-the-art ultrasonic imaging system is shown in Figure 1.1 (a), with its block diagram shown in Figure 1.1 (b). The system has three modules: the transducer arrays, the processing unit, and the image reconstruction unit. The transducer array is connected to the processing unit, which contains a transmitter pulser, a low-noise preamplifier (LNA), a time-gain controlled amplifier (TGC), a low-pass filter, and an analog-to-digital converter (ADC) for each channel. Transmit and receive beamforming units are located in the processing unit. The image reconstruction unit is composed of image processing electronics and the display.

(a) (b)
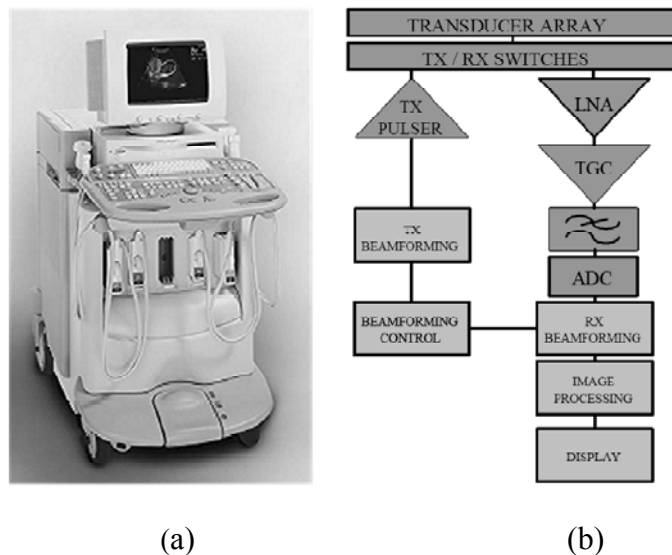
Figure 1.1. (a) A commercial state-of-the-art ultrasonic imaging system. (b) The block diagram of the imaging system.

In recent years, researchers have developed 3-D ultrasound imaging technology. It offers several advantages over 2-D ultrasound including improved elevational focusing, viewing planes that are usually inaccessible using 2-D ultrasound, volume-rendered images, more accurate volume measurements and improved detection of cystic or cancerous masses. Visualization using 3-D ultrasound can improve the detection of breast lesions, prostate cancer monitoring cardiac function and peripheral blood vessels.

2

Non-invasive imaging of blood vessels from outside the body is desirable. However, such an imaging process is only limited to the vessels close to the surface of the skin, for example, carotid arteries are routinely examined non-invasively using a linear array ultrasound transducer. The size and proximity of other vessels like the coronary arteries makes it impossible to image them non-invasively with acceptable resolution. The most common appearing of atherosclerosis is a rising constriction of the blood vessels affecting blood flow. Generally, the structural change caused by luminal narrowing is observed through angiographic images of the artery and stenosis has been a standard diagnostic indicator of the disease. However, the ability of X-ray angiography to detect vulnerable plaques is minimal [2]. These radiographic images present a view of the vessel with no clear information on the type and content of the plaque. Therefore, catheter based invasive imaging of the arterial cross-section with high resolution is gaining importance. Moreover, the catheter based techniques could also be used to guide cardiac interventional procedures. Common imaging techniques are being adapted for intravascular and/or intracardiac imaging.

1.2. Intravascular Ultrasound (IVUS) Imaging

IVUS is a catheter-based technique which uses ultrasonic imaging to produce images of the coronary artery from inside the lumen of the artery. IVUS is capable of providing real-time high-resolution images allowing tomographic assessment of lumen area, plaque size, and composition of a coronary segment, and therefore provides new insights into the diagnosis and therapy of coronary disease. The key to IVUS is a miniaturized transducer mounted on the catheter tip. Modern catheters typically are 2.9-Fr to 3.5-Fr (0.96 to 1.17 mm) in diameter. Currently, commercial IVUS systems are based on single element transducer or phased array transducer. In single-element IVUS catheters, the transducer is attached to the tip of the catheter and is continuously rotated at 30 rotations per second over 360 degrees. The center frequencies of these IVUS transducers are currently about 40 MHz [3]. In the phased-array IVUS catheter, a 64-element transducer is folded around the tip of the catheter and is electronically steered to acquire cross-sectional images over 360 degrees. The center frequency of these catheters is 20 MHz [4]. The IVUS imaging procedure using a single element and a phased array transducer is schematically explained in Figure 1.2.
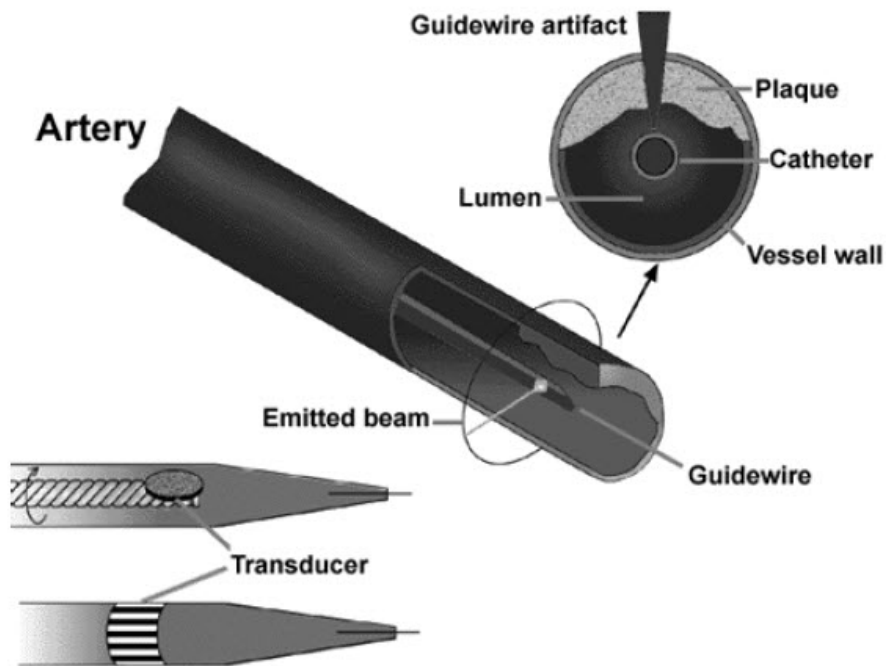
Figure 1.2. Schematic representation of IVUS catheter with transducers and plaque image in vessel [5].

1.3. Intracardiac Echocardiography Ultrasound Imaging

The use of intracardiac echo (ICE) imaging catheters for the guidance of interventional electrophysiology (EP) therapeutic procedures is becoming more common because of its features offering real time, direct observations and improved procedural guidance over that of fluoroscopy alone. The opportunity for applications of improved image guidance are certainly apparent in EP therapeutics. Atrial fibrillation itself, the most common cardiac dysrhythmia, now affects more than 2.2 million in the U.S. alone with 60,000 new cases each year. Current standard EP therapeutic guidance methods include fluoroscopy as the primary means to direct catheter position and movement, however EP ablation procedures can take as long as 3 hours, with long periods of radiation exposure. Methods are needed to improve clinical outcomes and reduce these undesirably long fluoroscopic exposures. Average exposure times of 22 minutes for isthmus ablation procedures to correct atrial flutter in the readily accessible right atrium are not uncommon, and the average fluoroscopy time during cardiac resynchronization device implantation procedures can be 35 minutes or longer. Extensive fluoroscopic exposures are hazardous for the

4

patient and practitioner alike. The technology and use of intracardiac echocardiography has progressed from the early days of the first experimental intracardiac probe built of 16 piezoceramic elements circumferentially arranged on a catheter tip. Electroanatomical mapping capability can be integrated into novel intracardiac imaging catheters to add yet another dimension to the image guidance equation for EP. Although there are several non-fluoroscopic guidance devices currently available, the NavX system has the very desirable ability to track in 3-D any EP catheter with standard plug connections, making it ideal for use with the available family of EP-ICE catheters. This feature makes the integration of 3-D spatial location and ICE imaging on a single catheter a very straight forward proposition [6].

The use of ICE not only reduces the risk of complications but also enhances the procedural success rate. ICE has also proven valuable in direct monitoring of acute procedure-related complications. For example, ICE can be used to monitor potential risks associated with ablation at the site of the pulmonary veins (PV), such as PV stenosis, thromboembolic complications, and perforation with pericardial tamponade. Phased-array ICE catheters have been available for several years now. A 10-Fr phased-array imaging catheter has been used in several animal and clinical studies since 2000 and in 2005 an 8-Fr version of the device (AcuNav, Siemens Medical Solutions USA, Inc., Mountain View, CA) was introduced. In these catheters, a piezoelectric transducer array is mounted on the side of the catheter for side-looking imaging. Limited available space and stringent packaging requirements challenge efforts to mount the transducer array at the tip of the catheter for forward-looking imaging, which is expected to enhance visualization in EP therapeutic interventions. The existing piezoelectric transducer fabrication technology relies on meticulous and labor-intensive steps such as hand lapping, polishing, and high-precision dicing. The capacitive micromachined ultrasonic transducer (CMUT) technology, however, takes advantage of mature silicon integrated circuit (IC) fabrication techniques, which make it possible to fabricate CMUTs of different shapes and sizes on a single wafer (i.e., 1-D array, 2-D array, ring array). The ease of fabrication also extends to CMUT devices for high-frequency applications such as intravascular ultrasound imaging, where a fine-pitch array of small elements is required. Compared with piezoelectric transducers, CMUTs offer wider bandwidth for improved resolution. Another

advantage of this technology is its seamless tight integration with supporting electronic circuitry that can be achieved either monolithically or through flip-chip bonding [7].

1.4. Motivation

IVUS is a useful tool for exploring arterial disease, guiding stent deployment and monitoring ablation procedures and is a catheter based imaging system which provides 2-D cross-sectional images as well as enables 3-D volumetric imaging [8-10]. Early Side-looking (SL) catheters with mechanically rotating single transducer provide 360° cross-sectional images of the vessel wall [11,12]. Later a more powerful SL probe was designed using circumferential arrays mounted around the catheter to enable electronic scanning of the cross-sectional area [13,14]. These probes provide high image resolution and are free of mechanical artifacts caused by rotating transducers. A SL probe has no forward looking capability to guide interventions. Therefore, a complimentary transducer system which enables forward-looking imaging through the vessel is needed.

Forward-Looking IVUS (FL-IVUS) catheters have volumetric imaging capability which is highly desirable in IVUS applications. A ring shaped array configuration is especially suitable for FL-IVUS since a guide wire is required in catheters. Besides the firstly designed piezoelectric single-ring transducers, CMUT based ring arrays were also realized [15]. The CMUT technology is promising for FL-IVUS imaging since it offers high bandwidth, good sensitivity and flexibility to fabricate arrays of different shapes and sizes. In addition, it enables monolithic or flip-chip-bonding-based electronics integration. By taking advantage of the flexibility offered by CMUT technology, it is possible to utilize the area around the guide wire efficiently by implementing multiple-ring arrays for FL-IVUS imaging. There have been several successful studies on implementing single and dual ring CMUT arrays for FL-IVUS [16]. Although the image quality of ring arrays is poor when compared with a full disk aperture, the previous studies show that it is a viable method for the implementation of a FL-IVUS.

FL-IVUS imaging system need to be small due to limited sizes on the front tip of IVUS catheters. This leaves a very small area for the array elements and front-end electronics. One of the main challenge in the array based FL-IVUS systems is the large channel count which results in increased system complexity. Synthetic phased array processing with reduced firing count simplifies the front-end and hence can enable 3-D real-time imaging. For the need to reduce the number of channels and/or firing count an optimization procedure has to be developed. The main objective of the optimization should be to discover a suitable array/firing configuration with an optimal image quality. For array optimization, several studies have been presented in the literature using both 2-D planar arrays and circular arrays. Most of them try to find sparse array layouts with optimized weighting schemes to reduce side lobes and suppress grating lobes in the beam pattern. Smith *et al.* used different transmit and receive arrays where grating lobes are suppressed by nulling transmit array response with receive array response [17]. Lockwood *et al.* introduced vernier interpolation with periodic but different transmit-receive arrays [18]. Austeng *et al.* proposed several sparse array designs with symmetric or asymmetric periodic and diagonal array configurations [19]. Holm *et al.* proposed optimized array distribution by using linear programming and simulated annealing algorithm for continuous wave far field approximation [20-22]. Later, Trucco extends this work for wideband 2-D arrays with applying both thinning and weighting by using simulated annealing and genetic algorithms [23,24]. All these approaches use full disk aperture or rectangular planar arrays and somewhat different from ring array structure. For the optimization of FL-IVUS single ring array, Wang *et al.* proposed to obtain optimal subset of all transmit-receive combinations by using element separation and interleaved arrangement strategy.

Another important challenge in FL-IVUS systems is low SNR due to the small array element sizes. 3-D real time imaging needs synthetic phased array. However, it causes low image SNR when compared with conventional phased array. Therefore, side lobe reduction by applying apodization or a custom weighting scheme are not desired to be used in the optimization of FL-IVUS arrays.

In this dissertation, we present optimized array designs for both circular and hexagonal ring arrays. The objective of the optimization is to obtain a predefined

number of optimal firing set which eliminates redundant spatial frequencies in the coarray (effective aperture) and produces low side lobe point spread functions (PSF). For this purpose, in this paper we used two different coarray sampling strategies and simulated annealing algorithm based optimizations.

1.5. Organization

This dissertation is organized in such a way that the following three chapters give some fundamental information for the reader to understand the results presented in succeeding chapters.

Chapter 2 explains the basic principles of ultrasonic imaging. The basic principles presented in this chapter include wave propagation, pulse-echo imaging, and wave properties of ultrasound.

Chapter 3 introduces the ultrasound array imaging principles. This chapter explains beamforming concept, modes of imaging, array and scan types, transducer types and some signal processing and mathematical relations of beam pattern, coarray and image formation.

Chapter 4 explains the imaging quality factors and resolution metrics. Simulated annealing algorithm technique and its features are explained in detail in chapter 5.

In Chapter 6 and Chapter 7, the proposed dual circular and dual hexagonal ring structures and optimization studies are presented in detail. The simulation results are demonstrated to test the proposed designs. Finally, the thesis ends with a conclusion and summary.

Chapter 2

Basics of Ultrasound Imaging

2.1. Ultrasound Physics

Ultrasound is a sound wave with frequencies higher than the upper limit of human audible range of 20 kHz. Unlike electromagnetic waves, ultrasound requires a medium to travel and it cannot propagate in vacuum. The wave propagates with the compression and rarefaction of the medium. The displacement plotted with respect to time gives a sinusoidal wave. The propagation velocity of the sound in medium is

$$c = \lambda f, \tag{2.1}$$

where λ is the wavelength, and f is the frequency. The average velocity in soft tissue is 1540 m/s.

2.2. Pulse-Echo Imaging

All ultrasound imaging systems in clinical use today rely on pulse-echo (A-scan) imaging. The basic principle of pulse-echo imaging is sending an excitation pulse from a transducer and receiving the reflected pulse signals from the tissues consisting of layers with different acoustic impedances. These reflections are converted into an electrical signal and the resulting signal is processed and displayed. The characteristics of the return signal (amplitude, phase, etc.) provide information about the nature of the interaction, and they give some indication of the type of medium in which they occurred.
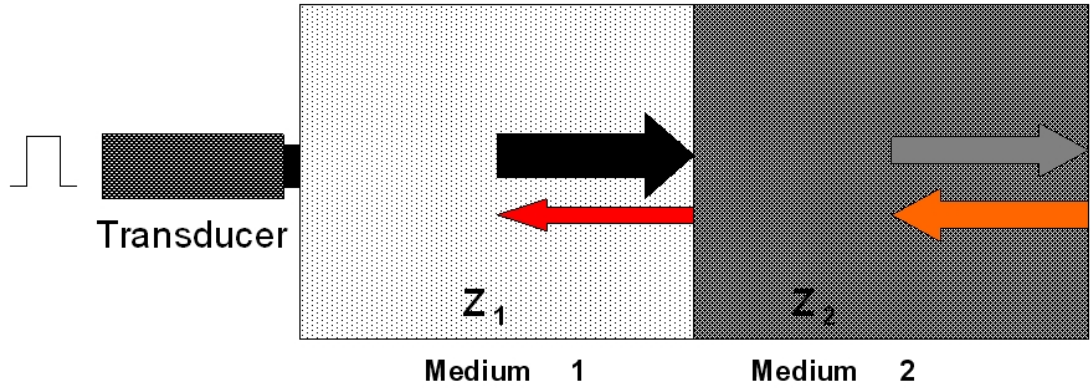
Figure 2.1. Pulse-Echo imaging.

An ultrasound wave propagates through a uniform medium without any change. When it encounters discontinuities and non-uniformities, part of the acoustic energy gets reflected and the remainder gets transmitted. The reflection depends on the difference between the characteristic impedances of the two materials. Assuming that the direction of acoustic propagation is perpendicular to the boundary between the two medium, the reflection coefficient R_m is defined as:

$$R_m = \frac{Z_2 - Z_1}{Z_2 + Z_1} \qquad (2.2)$$

where Z_1, Z_2 are the specific acoustic impedances of the material that the acoustic signal is traveling in and the next material respectively. R_m varies between -1 to 1. Negative values for R_m means the reflected signal is 180° out of phase with the incident signal. If $Z_2 = Z_1$ (the wave is traveling in the same medium) then $R_m=0$ and there will be no reflected wave. If $Z_2 \gg Z_1$ then $R_m \approx 1$ which means most of the signal will be reflected back when there is a big mismatch between the impedance of the media. For plane waves, the specific acoustic impedance is defined as:

$$Z = \rho c \qquad (2.3)$$

where ρ and c are the density of the material and speed of sound in the material respectively.

In diagnostic ultrasound imaging, sound waves are transmitted through biological tissue. The reflected acoustic signals are collected and converted to electrical signals. The amplitude of the electrical signals cause a corresponding increase or decrease in the brightness of the displayed image and the total transmit time from the initial pulse transmission to the reception of the echo is proportional to the depth of the boundary which can be determined by the following relationship

$$R = \frac{ct}{2}$$
(2.4)

where R is distance and t is time of arrival.

2.3. Ultrasound Properties

The most essential fact of medical ultrasound physics is that acoustic energy is transported through tissue as a sound wave. This acoustic wave propagates by longitudinal compression. Because it is a wave, ultrasound is subjected to all the wave-like behaviors of classical physics like scattering, refraction, attenuation, and diffraction.

2.3.1. Reflection, Refraction and Scattering

When an ultrasound transducer emits sound energy into the body, it travels through tissue unimpeded until it scatters from the abrupt changes in acoustic impedance at the interfaces between different tissue types. Some of the sound is scattered back to the transducer to be received and processed to extract information, while the remainder travels on and to the next reflector and so on. Thus, the reflection property of sound makes ultrasound imaging possible.

Wave refraction is a change in direction of the wave as it travels through tissue which is caused by change in the sound velocity in the tissue. This phenomenon can cause image distortions, because the reflected ultrasound used to form an image may not travel in a straight line from transducer to target and back again.

Scattering is the result of reflection. Each small tissue volume which contains tissues of two or more impedances is a scattering center. If the characteristic size of the scatterer is small compared to the ultrasound wavelength, as in the case of red blood cells, then the sound energy is scattered uniformly in all directions. This is called diffuse scattering and the energy reflected back to the transducer is small. If, on the other hand, the scatter site is comparable to the wavelength as in the case of a vessel wall, then the energy is reflected mostly at an angle equal to that of incidence. This is called specular scattering and the reflected energy can be large or small depending of the incident angle.

2.3.2. Attenuation

As the ultrasonic beam travels through the medium, the wave intensity is attenuated. Attenuation is caused by local energy absorption, reflection, scattering, etc. Absorption is the local conversion of ultrasound wave energy to other energy forms, mostly heat. Attenuation constant can be modeled as

$$\mu(f) = \alpha f^{\beta} \tag{2.5}$$

α and β are acoustic parameters of the medium, and f is the transducer center frequency. Equation (2.5) shows that the attenuation is proportional to the center frequency for $\beta=1$. Consequently, higher frequency ultrasound transducers result in an increase of attenuation. In human tissue, typical values for α, β are $\beta =1$ and $\alpha = $ 1dB/cm/MHz [25]. Attenuation of tissues is significant and limits not only the depth of penetration but the spatial resolution as well.

2.3.3. Diffraction

Another important phenomenon that occurs during wave propagation is diffraction. Diffraction refers to a bending of light rays when a wave encounters an obstacle. It is described as the deviation of a radiated beam from rectilinear paths that cannot be interpreted as reflection or refraction. Similar effects are observed when light waves travel through a medium with a varying refractive index or a sound wave through a medium with varying acoustic impedance. Diffraction occurs with all waves,

including sound waves, water waves, and electromagnetic waves such as visible light, x-rays and radio waves.
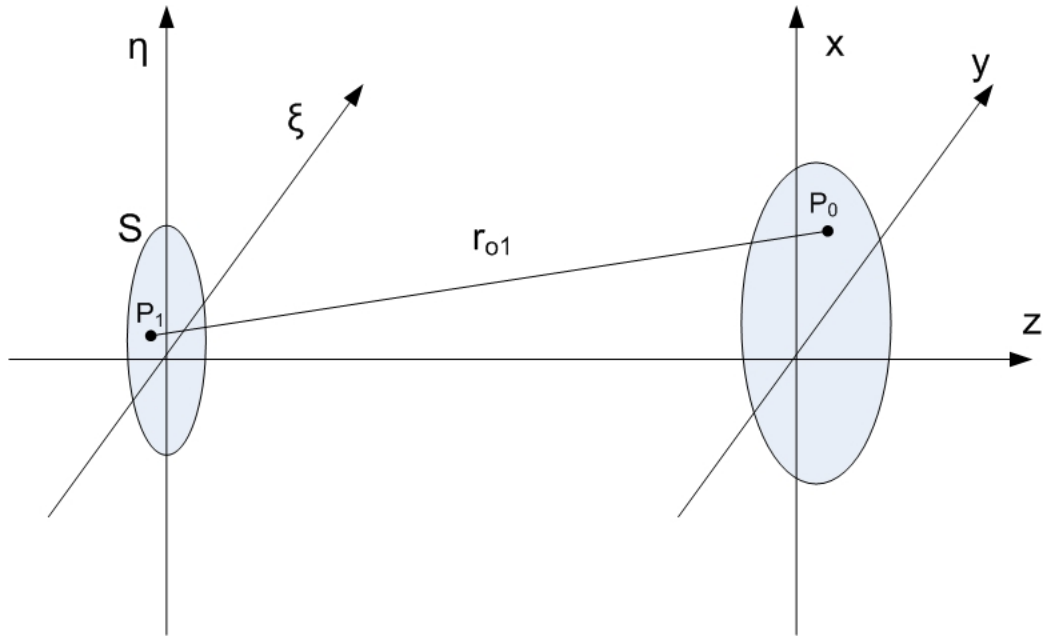
Figure 2.2. Diffraction geometry.

The theory of diffraction explains why plane waves deviate from their straight line propagation when passing through an aperture. The effect of diffraction on a propagating wave depends on the size of the aperture. A small aperture spreads the wave field. Christian Huygens tried to explained this phenomena. Huygens' Principle states that each point on the surface of the aperture is the origin of a spherical wave and additionally, the advancing wave as a whole may be regarded as the sum of all the secondary waves arising from points in the medium. The wave field can then be calculated from the Rayleigh-Sommerfeld diffraction formula, which for acoustic waves takes on the form [26]

$$U(P_0) = \frac{1}{j\lambda} \iint\limits_{S} U(P_1) \frac{e^{jkr_{01}}}{r_{01}} cos\theta dS, \qquad (2.6)$$

13

where θ is the angle between the normal vector n and the vector r_{01} pointing from P_0 to P_1. The term $cos\theta$ is given by

$$cos\theta = \frac{z}{r_{01}} \tag{2.7}$$

and therefore the Huygens-Fresnel expression can be written as

$$U(x,y) = \frac{z}{j\lambda} \int \int_S U(\xi,\eta) \frac{e^{jkr_{01}}}{r_{01}^2} d\xi d\eta \tag{2.8}$$

where the distance r_{01} can be calculated as

$$r_{01} = \sqrt{z^2 + (x-\xi)^2 + (y-\eta)^2} \tag{2.9}$$

To reduce the Huygens-Fresnel principle to a more simple and useful expression, two different approximations for the distance r_{01} between P_0 and P_1. The approximations are based on the binomial expression of the square root. The condition for the distance z that satisfies,

$$z^3 \gg \frac{\pi}{4\lambda}[(x-\xi)^2 + (y-\eta)^2]^2_{max} \tag{2.10}$$

results in the Fresnel approximation and modifies the Huygens-Fresnel expression yielding,

$$U(x,y) = \frac{e^{jkz}}{j\lambda z} e^{j\frac{k}{2z}(x^2+y^2)} \int\int_{-\infty}^{\infty} \left\{ U(\xi,\eta)e^{j\frac{k}{2z}(\xi^2+\eta^2)} \right\} e^{j\frac{2\pi}{\lambda z}(x\xi+y\eta)} d\xi d\eta \tag{2.11}$$

which is equivalent to the Fourier transform of the product of the complex field of the radiating aperture and a quadratic phase exponential. Equation (2.11) is referred to as the Fresnel diffraction integral.

If an additional condition to the Fresnel approximation given as

$$z \gg k \frac{(\xi^2 + \eta^2)_{max}}{2} \qquad (2.12)$$

is satisfied, then the quadratic phase factor under the integral in Equation (2.11) is approximately unity over the entire aperture, and the observed field strength can be found directly from a Fourier transform of the aperture distribution itself. Therefore the diffraction field in the region of Fraunhofer or the far field can be expressed as,

$$U(x, y) = \frac{e^{jkz}}{j\lambda z} e^{j\frac{k}{2z}(x^2 + y^2)} \iint\limits_{-\infty}^{\infty} U(\xi, \eta) e^{j\frac{2\pi}{\lambda z}(x\xi + y\eta)} d\xi d\eta \qquad (2.13)$$

where $x/\lambda z$ and $y/\lambda z$ correspond to the spatial frequencies of the 2-D Fourier transform. The Fraunhofer approximation will be valid provided

$$z > \frac{D^2}{\lambda} \qquad (2.14)$$

where D is the linear dimension of the aperture. The inequality is also often used to define a boundary between the near and far fields of the aperture.

In the near-field, the beam is a cylindrical extension of the transducer. In the far-field the beam expands with a fixed opening angle. Between these two regions there is a transition region called focal zone in which the beam contracts before starting to expand. In the far-field the beam is composed of a central main lobe and side lobs around this. The beam can be focused by giving a spherical shape to the transducer. This will improve the resolution of the system.
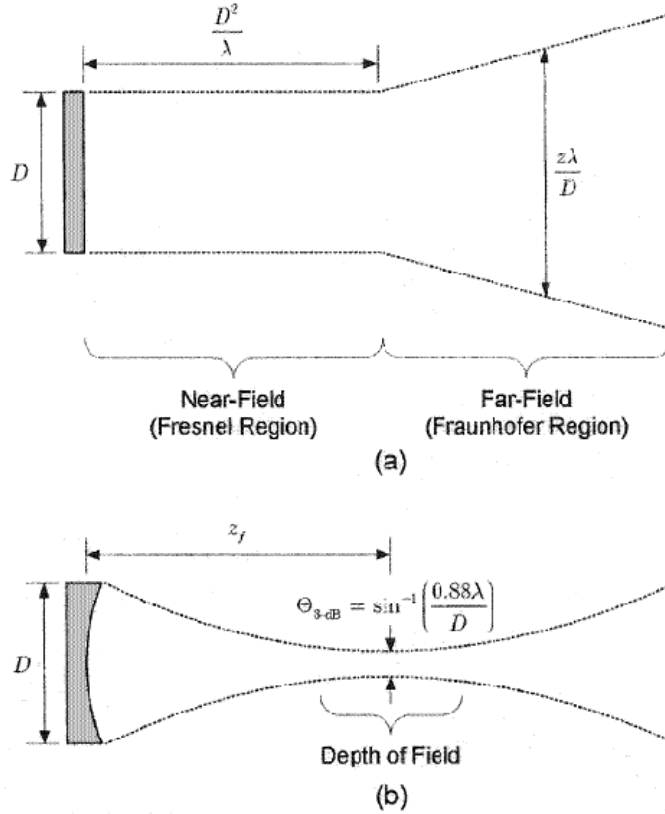
Figure 2.3. Beam patterns of (a) an unfocused transducer and (b) a focused transducer [27].

The focused beam becomes narrower at the focal point and spreads out beyond the focal point. An important metric that defines the lateral beam width of a focused imaging system is 3-dB width of the beam at the focal point. For a rectangular aperture the 3-dB beam width is expressed as

$$\theta_{3dB} = \sin^{-1}\left(\frac{0.88\lambda}{D}\right) \tag{2.15}$$

where D is the width of the aperture and λ is the wavelength [45]. As the beam width is proportional to aperture size and wavelength, the lateral resolution can be improved by using large apertures and high frequency.

For a focused array another simplification on Huygens-Fresnel principle to find the array field on a sphere passes through the focal point. Hence, the distance between the aperture surface and the observation surface can be defined as [27]:

$$r_{01} = z_f - \frac{x\xi}{z_f} - \frac{y\eta}{z_f} \qquad (2.16)$$

Substituting the equation in Huygens-Fresnel principle of Equation (2.8), one gets the following Fresnel approximation,

$$U(x, y, z_f) = \frac{e^{\frac{j2\pi}{\lambda}z_f}}{j\lambda z_f} \int \int U_s(\xi, \eta) e^{-\frac{j2\pi}{\lambda z_f}(x\xi + y\eta)} d\xi d\eta \qquad (2.17)$$

If we express the above equation in polar coordinates by neglecting the phase term, we obtain the integral equation as 2-D Fourier transform of the aperture function:

$$U(\theta_x, \theta_y; r) = \frac{1}{\lambda r} F\{U(\xi, \eta)\}\Big|_{f_x = \frac{\sin\theta_x}{\lambda}, f_y = \frac{\sin\theta_y}{\lambda}} \qquad (2.18)$$

The similarity of the above equation with the Fraunhofer approximation, shows that focusing brings the far field behavior into the near field.

Chapter 3
Ultrasound Array Imaging

Single element transducers have fixed focus and need to be mechanically scanned (or acoustic lens) to obtain a cross-sectional image for the tissue. The acoustic lens or mechanical scanning of a 1-D array focuses the beam at a single, predetermined depth. The beam is well focused in elevation at this depth, but diverges at depths away from the focus degrading the image quality due to the increase in slice thickness. Electronically controlled beam forming can be obtained by using an array of transducer elements. According to Huygens-Fresnel principle each array element generates a wave that will interfere and form a resulting beam.

3.1. Beamforming

Transducer arrays are sets of individually controlled elements used to give sets of 1-D image lines that are processed and grouped together to give a 2-D or 3-D image. They have the advantage of electronic steering and focusing of the acoustic beam which gives a wider view far away from the transducer. This results in an improvement on image quality and frame rate. Steering is performed by time delays and to focusing is performed by applying phase delays to the transmitted and received signals as shown in Figure 3.1 (a) and (b). The combination of these two delays as shown in Figure 3.1 (c) is called beamforming.

The simplest beamforming algorithm is called delay-and-sum beamforming. Since the distance from the focal point to the elements is different, the echo signals reflected from the target arrive to the elements at different times.
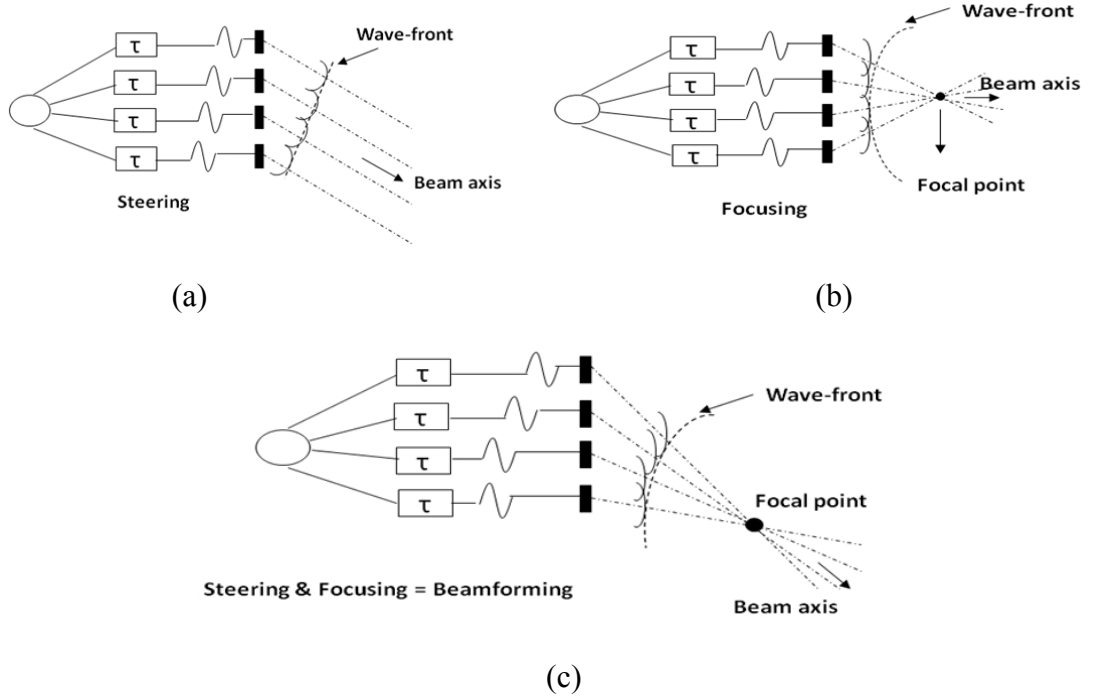
Figure 3.1. Schematic description of beamforming, (a) beam steering, (b) focusing, (c) beamforming.

As a result of beamforming the received signal $r(t)$ can be obtained by applying time delays to the signals according to the following expression:

$$r(t) = \sum_{i=1}^{N} w_i \sum_{j=1}^{N} w_j s\left(t - \frac{2R_f}{c} - \tau_i - \tau_j\right) \tag{3.1}$$

where w_i and w_j represent the apodization weights of transmit and receive, respectively. $s(t)$ is the excitation pulse signal, τ_i and τ_j are the phase delays of the transmit and receive beamformers, respectively. R_f is the distance of focal point to the array center. The phase delays can be found as,

$$\tau_{i,j} = \frac{\sqrt{(x_{i,j} - x_f)^2 + (y_{i,j} - y_f)^2 + (z_{i,j} - z_f)^2}}{c} - \frac{R_f}{c} \tag{3.2}$$

where $x_{i,j}$, $y_{i,j}$ and $z_{i,j}$ are the coordinates of array element locations, x_f, y_f and z_f are the coordinates of focal point and c is the speed of sound. If a focal point is a fixed

point in the space then the beamforming is fixed focus and if the focal point is dynamically moving then the beamforming is called dynamic focusing.

3.1.1. Phased Array Beamforming

For a conventional phased array (PA) imaging system, all elements transmit simultaneously sound waves to generate a pre-focused beam. The pre-focused beam is transmitted into the imaging space at a particular direction. Received RF data is delayed for focusing and summed to produce a single line of pulse-echo data. Then a pre-focused transmit beam is fired to a new direction to form a new image line. After the transmit beam fully scan a sector, a 2-D polar image is generated. In phased array, steering and focusing is simultaneously performed in both transmit and receive operation. The main advantage of phased array is high image resolution. However, as all the transmit and receive channels are simultaneously used in image formation, the complexity of the system is excessive. Especially for large arrays, the system is impractical to design [28].

3.1.2. Synthetic Array Beamforming

Due to the drawbacks of conventional PA system, the idea of synthetic array (aperture) system has been developed. In conventional synthetic aperture (CSA) system, at each time only single element is active in transmit and receive operation. All RF data is recorded when all transmit-receive operation is completed in the array. Unlike with PA imaging where all elements are fired to form a narrow beam on a scan line, CSA imaging results in a wider beam that illuminates a large part of the imaging medium. This means that received signals contain echo signals from all the reflectors in a large imaging medium. By applying proper delays and summing the received signals, a 2-D sector image is formed. Although, CSA reduces system complexity in large arrays, the resolution as well as SNR is reasonably reduced.

To increase image quality, synthetic phased array (SPA) that combines the principles of PA and CSA is developed. In SPA, as in the case of CSA, in a particular time only single element is used in transmit and receive operation but this time the transmit channel is fixed until all receive elements have been used once in reception.

Consequently, all Tx-Rx firing combinations are realized and an improved image quality is provided. Although, SPA increases image quality and reduces system complexity/cost, it still suffers from low SNR and, due to the large number of firing events, reduction in frame rate [29].

3.2. Beam Pattern

Beam pattern of an imaging system is the radiation pattern of transducer. As explained in the previous section for far-field approximation it is the Fourier transform of the aperture function. Consider a linear continuous aperture of width *D* as shown in Figure 3.2. The aperture function *a(x)* represents the amplitude and phase distribution on the aperture surface. Suppose the aperture has uniform weighting representing a rectangular window with unit height, thus the 1-way beam pattern in rectangular and polar coordinates can be found as,

$$U(x,y) = F\{a(x)\} = \int_{-\frac{D}{2}}^{\frac{D}{2}} e^{-\frac{j2\pi}{\lambda z}x\xi} d\xi = \frac{sin\frac{\pi}{z\lambda}Dx}{\frac{\pi}{z\lambda}Dx} \quad and$$

$$U(\theta) = \frac{\sin\left(\frac{\pi}{\lambda}Dsin(\theta)\right)}{\frac{\pi}{\lambda}Dsin(\theta)} = sinc\left(\frac{\pi D}{\lambda}\sin(\theta)\right), \tag{3.3}$$

respectively, where λ is the wavelength, *a(x)* is the aperture function which is equal to *rect(D)* and *D* is the aperture size. It can be seen in Equation (3.3) that the normalized beam profile of a continuous aperture with uniform amplitude results a *sinc* function as expected. If same aperture is used both in transmit and receive then the two-way beam pattern is equal to the square of one-way beam pattern:

$$U_{TR}(\theta) = sinc^2\left(\frac{\pi D}{\lambda}\sin(\theta)\right) \tag{3.4}$$
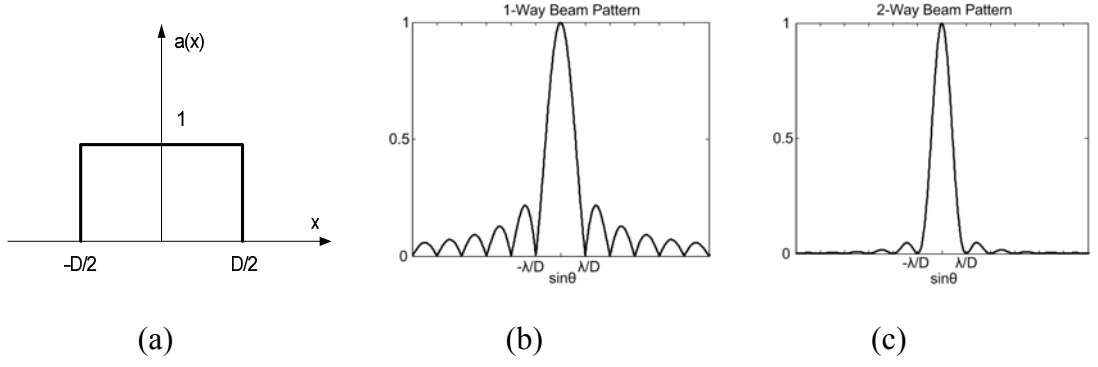
Figure 3.2. (a)1-D continuous aperture, (b) 1-way beam pattern and (c) two-way beam pattern.

If we sampled the continuous aperture to form an array composed of elements of size ω and aligned in the x direction as shown in Figure 3.3 (a), the discrete aperture function can be represented as,

$$s(x) = rect(D)\left[rect(w) * \sum_{n=-\infty}^{\infty} \delta(x-n)\right],\qquad(3.5)$$

where the symbol '*' represents the convolution. The far-field two-way beam pattern of a linear array can be found by taking the Fourier transform of Equation (3.5) and can be expressed as,

$$S(\theta) = \left[\frac{\sin\left(\frac{N\pi d}{\lambda}\sin\theta\right)}{\sin\left(\frac{\pi d}{\lambda}\sin\theta\right)}\right]^2 \left[\frac{\sin\left(\frac{\pi\omega}{\lambda}\sin\theta\right)}{\frac{\pi\omega}{\lambda}\sin\theta}\right]^2 \cos^2\theta \qquad(3.6)$$

where N is the number of array elements and d is the inter-element distance. The expression has some meaningful difference from the continuous array beam pattern. The first term is the periodicity coming from discrete array elements, the second is due to the finite size of array elements and the last is the obliquity factor.

22
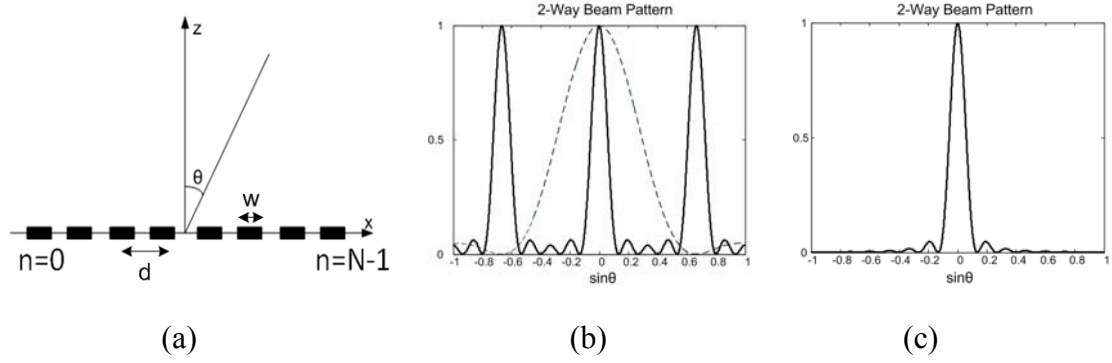
Figure 3.3. (a) Linear array geometry, (b) the two-way beam pattern of first term (solid line), second term (dashed line), (c) the overall two-way beam pattern.

The unsteered beam pattern of a linear array where $d=1.5\lambda$ is shown in Figure 3.3. Due to the relation between sampled aperture and the beam pattern, sampling the aperture produces periodic replicas on the beam pattern, as shown in Figure 3.3 (b). These replicas are called grating lobe which means unwanted aliases. Grating lobe causes distortion in visible region, on the beam pattern due to undersampling of the aperture. The second term in the beam pattern, which is called the element factor, cancels these grating lobes when we choose $w=d$. To eliminate the grating lobes independent of the element factor, one may choose $d=\lambda$ so that the grating lobes are pushed beyond $\pm\pi/2$ which means the range of the visible region.

The steered beam pattern will shift the main lobe from the beam pattern center as well as the grating lobes. That means choosing the element pitch λ would not guarantee elimination of the grating lobes. To avoid grating lobes in the visible region for steering angles up to $\pi/2$, the array must be sampled with a period less than half wavelength:

$$d < \frac{\lambda}{2} \qquad (3.7)$$

This is due to the Nyquist sampling criterion, and refers to critically sampled array.

23

3.3. Effective Aperture (Coarray)

As mentioned in the previous sections, the two-way beam pattern of an aperture is equal to the multiplication of the one-way beam patterns of transmit and receive aperture. Due to the Fourier transform properties, multiplication in Fourier domain results in a convolution in spatial domain. That means we can define a new aperture function which is the convolution of transmit and receive apertures so that the one-way beam pattern of this new aperture is equivalent to the two-way beam pattern of the aperture. The defined aperture is called effective aperture and expressed as,

$$a_{TR}(x) = a_T(x) * a_R(x) \tag{3.8}$$

and the one-way beam pattern of effective aperture is given as,

$$U_{TR}(\theta) = U_T(\theta) \cdot U_R(\theta) = F\{a_{TR}(x)\} \tag{3.9}$$

The overall two-way beam pattern represents the combination of transmit and receive response of the aperture. Because the response of a pulse-echo ultrasound system depends on both transmit and receive beam patterns, the term is often represented by a single function called two-way point spread function (PSF) and it is equivalent to $U_{TR}(\theta)$.

The PSF can be defined as the response of an imaging system to a point which is a reflector in space and totally characterizes the imaging ability of the system. Thus, the real image of an imaging medium can be found by the convolution of PSF and the reflectivity function of imaging space. That means the ideal PSF is an impulse function so that the image would be equal to the reflectivity function. Because the PSF is a function of angle, the lateral resolution will increase as a function of radius. And also wider aperture width results in a narrower PSF which causes the resolution to increase.

The term *effective aperture* can be used interchangeably with *coarray*, which is in fact the scaled version of effective aperture and represents the spatial frequency response of the transmit/receive imaging system. Because the coarray has a Fourier transform relation with PSF, it also completely characterizes the imaging system.

During the rest of the thesis we use the coarray definition for our design and system analysis.

3.4. Beam Sampling

In reconstruction of the beam space, we should consider the Nyquist sampling criterion to define minimum beam sampling interval. For the rectangular aperture case size *D*, the effective aperture has a width of *2D* resulting a *sinc²* form of PSF. The spatial frequency bandwidth that means the width of the coarray is equal to *2D/λ*. The minimum spatial sampling frequency should be two times the spatial sampling frequency. Consequently, the required spatial sampling interval should be defined as,

$$\Delta \sin(\theta) = \frac{\lambda}{2D}$$

(3.10)

so that the beam pattern can be reconstructed from the beam samples. If the image scans a sector angle of θ_s, then the minimum number of beams should be expressed as [30],

$$Q = \frac{2D}{\lambda}\left(2\sin\left(\frac{\theta_s}{2}\right)\right)$$

(3.11)

The spatial sampling frequency along the beam direction is related to the sampling frequency of the temporal echo signals. The critical sampling frequency for the echo signals is twice the largest frequency component of the echo signals. Due to two-way signal propagation the critical temporal sampling frequency is reflected as *λ/4* minimum spacing of dynamic focal points along a beam line [31].

3.5. Imaging Modes

There are several modes of ultrasound used in medical imaging. A-mode is the simplest type of ultrasound imaging. In this mode a transducer scans a line through the body with the echos plotted on the display as a function of depth.

In B-mode imaging, array of transducers simultaneously scans a plane through the body that can be viewed as a two-dimension cross-sectional image on the display. It is the mostly used ultrasound imaging modality.

In M-mode imaging which means "motion mode", a rapid sequence of B-mode scans whose images follow each other on screen enables to see and measure range of motion, as the organ boundaries that produce reflections move relative to the probe.

The Doppler mode is used to measure and visualize the blood flow. In color Doppler, the velocity information is presented as a color coded overlay on top of a B-mode image. In continuous Doppler, the information is sampled along a line through the body, and all velocities detected at each time point is presented (on a time line). In pulse Doppler, information is sampled from only a small sample volume (defined in 2-D image), and presented on a timeline.

3.6. Transducers

The key component of an ultrasound transducer is the element which transmits and receives sound energy. During transmit, this element converts electrical to mechanical energy. In the receive mode, the returning acoustic wave is converted by the element to an electrical signal, and then routed to the receiver electronics. Frequently used transducer type is piezoelectric type. The piezoelectric element can be made from a variety of materials. Barium titanate was the first to be discovered. Today PZT (lead zirconate titanate) ceramic is the most commonly employed due to its high electrical-to-mechanical coupling coefficient (ECC), high dielectric permittivity and low dielectric losses. The limitations of PZT such as high acoustic impedance and the lack of mechanical flexibility, have led to an interest in copolymer and polymer materials, such as polyvinylidene fluoride (PVDF) provide a good acoustic match to tissue but exhibit a poor electrical-to-mechanical coupling efficiency which has limited the applications of these materials in medical imaging. Composites have good electrical-to-mechanical coupling. They can be matched acoustically to tissue, and can be flexible enough to be formed into a variety of shapes [32].

Piezoelectric transducers have long dominated ultrasonic transducer technology, but CMUTs have recently emerged as an alternative offering advantages such as wide bandwidth, ease of fabricating large arrays, and potential for integration with supporting electronic circuits. CMUT technology can potentially produce the type of integrated catheter arrays and external probes enabling advanced 3-D imaging. A CMUT is simply a device with two plate-like electrodes biased with a DC voltage and driven with an additional AC signal to harmonically move one of the plates. The main components are the cavity, the membrane, and the electrode. Using common IC fabrication processes, a capacitor cell appears as a metalized membrane (top electrode) suspended above a heavily doped silicon substrate (bottom electrode), as shown in Figure 3.4. An insulating layer is included to prevent the two electrodes from shorting in case of contact. A single transducer element uses many small capacitor cells connected in parallel. By organizing transducer elements in different geometries, any array shape is possible [33].
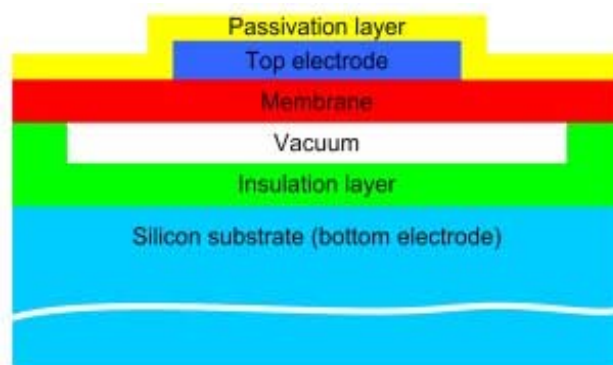
Figure 3.4. Basic CMUT structure.

CMUTs provide several advantages over piezoelectric transducers: they can be batch-produced with micromachining processes to tight parameter specifications, which is difficult for piezoelectrics; they are easier to fabricate than piezoelectric transducers; batch processing also enables the fabrication of transducer arrays with different geometries and operating frequencies on a single wafer. The use of standard IC processes also makes integration of CMUT arrays with supporting electronics convenient and CMUTs can operate over a wider temperature range than piezoelectric devices. Results over the last decade demonstrate that traditionally fabricated CMUTs optimized with respect to such design parameters as device size,

27

membrane radius, thickness, shape, gap height, and operating mode compare favorably to piezoelectric transducers in terms of bandwidth (170%), frequency range (100 kHz-70 MHz), dynamic range (130 dB/V), maximum output pressure (35 kPa/V) and receive sensitivity (50 dB/Pa/Hz) [33].

3.7. Scan Conversion

After a beam is scanned over a cross-section of an object, a polar image with vertical axis as range r and horizontal axis as angle θ is formed. Scan conversion is necessary to convert from polar coordinates associated with the ultrasound data to the Cartesian coordinates. The Cartesian image is an image space divided by small and rectangular regions called pixels. The pixel size is set by the desired resolution of the image. The value of each pixel (x,y) can be obtained by using an output-to-input mapping. A pixel is first identified in the Cartesian image. Its coordinates are then mapped to a fractional pixel location in the polar image. For each pixel (x,y) in the Cartesian image, the corresponding position in the polar image can be obtained by following equations:

$$r = \sqrt{x^2 + y^2} \qquad (3.12)$$

$$\theta = \arcsin\left(\frac{x}{r}\right) \qquad (3.13)$$

the signal value at the (r,θ) position is then obtained by interpolation. There are many interpolation methods. Mostly used one is bilinear interpolation. Representation of the method is shown in Figure 3.5. The interpolation transforms amplitude samples on the polar scan lines, to the corresponding pixel in Cartesian coordinate system. For a particular image pixel four sampled data points are used for the interpolation. The pixel value is determined by a weighted average of the sampled values [32].
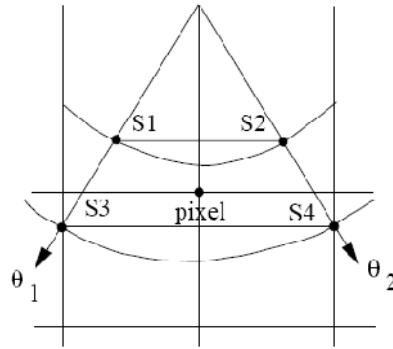
Figure 3.5. Scan conversion with bilinear interpolation.

3.8. Gain Compensation

The ultrasound energy is attenuated when traveling through the medium. Two identical targets at different depths will produce echoes of different amplitude. The echoes produced by the closer target are stronger. In order to solve this problem, the time-gain compensation (TGC) is used. In this method, the gain of the amplifier is increased as a function of depth to compensate for the loss in energy. Various forms of TGC, such as exponential, linear and windowed TGC are available.

3.9. Logarithmic Compression

Logarithmic compression helps in reducing the dynamic range of the B-scan images for display on a monitor as well as enhancing weak backscatterers. In most imaging systems, the amplitude of the raw signal from the object is compressed so that weak targets are visualized together with the strong targets. All images shown in this thesis are compressed by logarithmic compression which is defined by

$$z_c(t) = 20 \log_{10}(z(t)) \qquad\qquad 3.14$$

where $z(t)$ and $z_c(t)$ are the linear and compressed envelopes, respectively.

Chapter 4
Image Quality Factors

4. 1. Axial Resolution

Axial or range resolution refers to the ability of the system to separate objects located along the propagation axis of the ultrasound beam. It is determined by the shape and length of the transmitted pulse and is inversely proportional to the pulse bandwidth BW. The axial resolution is [34]

$$\Delta r = \frac{c}{2BW} \tag{4.1}$$

where c is the propagation speed. Consequently, higher frequency produce short pulse resulting improved axial resolution. However, increasing frequency results in a decrease in penetration due to the frequency dependent attenuation. Therefore, a tradeoff between penetration depth and axial resolution should be resolved.

4.2. Lateral Resolution

Lateral resolution is used to measure the ability of an imaging system to separate objects located perpendicular to the beam axis. It is primarily determined by the beam width of the transducer. It is also governed by the shape of the sound which, in general, is characterized by the aperture (determined by number of elements and pitch), the transmitting frequency and by focusing of the transducer. For phased arrays, the beam in the scan plane is focused electronically. The 6-dB lateral resolution of a transducer can be approximated by,

$$6 - dB\ Lateral\ Resolution = \frac{1.02\lambda R}{D_A} \tag{4.2}$$

where λ is the wavelength, R is the range from the transducer surface and D_A is the diameter of the transducer [34]. Increasing frequency and aperture size result in a better lateral resolution.

4.3. Contrast Resolution

Contrast resolution can be defined as the smallest difference in tissue acoustic impedance which can be resolved and displayed as two different gray levels in the image. Adequate contrast resolution is essential for the tissue discrimination required for diagnostic ultrasound imaging. The primary factors influencing contrast resolution are spatial resolution, systems dynamic range, sidelobe level, and image noise. Detection of high contrast targets is limited by the imaging system's spatial resolution. Reduced sidelobe levels can also result in a better contrast resolution. Sometimes the contrast resolution is referred to as the dynamic range of the image which is defined as the ratio of the strongest signal to the weakest signal, often presented in dB.

4.4. Temporal Resolution

Temporal resolution is defined as the ability to resolve movements of structures in the image. The primary determinant of the temporal resolution is the time required to form an image and usually refers to frame rate which is the number of images per unit time and usually expressed in terms of frame per second (fps). For synthetic phased array imaging, the time take for single firing of the two-way propagation time from the array to the imaging depth is equal to *2R/c*. If R is the image depth and N_f represents the number of firings to form a single frame, the frame rate is given by,

$$FR = \frac{c}{2RN_f} \tag{4.3}$$

Frame rate is an important issue in real-time imaging system. Low frame rate means that the movement of structures (e.g. heart valves) are not easily imaged and diagnosis may be failed.

4.5. Signal To Noise Ratio (SNR)

Signal-to-noise ratio (SNR) is a measure of the amount of signal information relative to the interfering noise which is always present in an image. If we consider the case for a single transducer element receiving signal from the medium, we can define received signal $r(t)$ as,

$$r(t) = s(t) + n(t) \tag{4.4}$$

where $s(t)$ represents the signal field and $n(t)$ represent the noise field. The noise caused by speckles in the medium and electronics is independent from the signal field. Therefore an additive noise model can be usually defined. The noise in the received signal is often zero-mean and described by its variance. Therefore, for array channel, the SNR can be defined as,

$$SNR = \frac{P_s}{\sigma_N^2} \tag{4.5}$$

where P_s represents the signal power and σ_N^2 represents the noise variance. To increase SNR, signal power should be increased and/or should be decreased noise power. Using large array elements and averaging of received signals improve SNR. The image SNR of a single point in the reconstructed image for PA system is generally expressed as,

$$SNR = 20 \log_{10}\left(N_T \sqrt{N_R}\right) + SNR_0 \tag{4.6}$$

where N_T and N_R are the number of active transmit and receive elements, respectively, and SNR_0 is the SNR of a single channel. The image SNR for CSA and SPA can be similarly defined as,

$$SNR = 20 \log_{10}\left(\sqrt{N_f}\right) + SNR_0 \tag{4.7}$$

where N_f is the number of firings to form a single image.

Chapter 5

Simulated Annealing

5.1. Combinatorial Optimization

Combinatorial optimization problems deal with finding an optimal solution among a finite number of solutions. The easiest ones are those that can be solved in polynomial time, i.e. the number of steps is bounded by a polynomial. These are said to belong to the *P*-class. The more general *NP*-class consists of those problems that can be solved in nondeterministic polynomial time.

A problem is said to be *NP*-hard if an algorithm that solves it can be used to solve any other *NP*-problem. If a problem belongs to the *NP*-class and is *NP*-hard it is said to be *NP*-complete. No method has been found for solving any *NP*-complete problem in polynomial time [35].

With the complicated relationship between the configuration of an array and its response it is a reasonable assumption that any optimization of an array response is an *NP*-hard problem. There is a common assumption that *NP*-hard problems can't be solved in polynomial time. Hence algorithms that can find near optimal solutions in reasonable time have received a lot of attention.

These algorithms, called heuristics, do not guarantee the quality of the solution found. In practice, many have been shown to be sufficient for a wide range of purposes, finding near-optimal solutions bounded by a polynomial time of low order. There are two types of these algorithms; constructive and local search algorithms.

Local search algorithms use a neighborhood function to find good solutions. Some examples of these algorithms include simulated annealing, tabu search, genetic algorithms and neural networks. They have gained popularity over recent years after

being put on a firm basis within a mathematical framework, thus enabling us to study the performance of the algorithms. With the arrival of fast computers solving large problems is now feasible. Since local search algorithms are flexible and easy to understand they are now being used on a wide range of problems.

A combinatorial optimization problem can be classified by the set of feasible solutions S and a cost function $f(.)$. The cost function (also called objective function) usually gives some sort of quantitative information on how good or bad a system behaves. It can depend on a great number of independent variables. The problem is to find the optimal solution $i^* \in S$ so that $f(i^*) \le f(i)$, for all $i \in S$. Then $f(i^*)$ is the optimal cost. Local search algorithms start with an initial solution and then try to find better solutions by searching the neighborhood for lower costs. The neighborhood function can be defined by $N(i)$. When a better solution is found in $N(i)$ it replaces the previous solution.

5.2. Simulated Annealing

Simulated annealing has been used with success on several combinatorial optimization problems, the most famous being the traveling salesman problem (TSP). With a list of cities, and a given cost for traveling between any two cities, the traveling salesman problem is finding a route passing through all the cities once only and at the same time minimizing the total cost. This is an *NP*-complete problem [36]. In addition simulated annealing has also been shown useful in other areas such as circuit design and image processing and, in our case, the optimization of arrays.

5.2.1. Analogy

Simulated annealing is a method which stems from statistical physics [37], where it is desirable that melted solids reach low-energy states when cooled down. Consider particles in a liquid state at a high temperature in a heat bath. We then begin a slow cooling process, where the temperature T is lowered through several stages. At each stage the solid is given time to reach thermal equilibrium. The probability of this state having an energy E is given by the Boltzmann distribution,

$$P(E) = \frac{1}{z(t)} e^{-E/(k_b T)} \tag{5.1}$$

$Z(t)$ is the partition function, $k_B = 1.38.10^{-23}$ J/K is the Boltzmann constant and the term $e^{-E/(k_b T)}$ is known as the Boltzmann factor. As the temperature is lowered the Boltzmann distribution moves the system towards the lowest energy states. When the temperature then tends to zero only the minimum energy state has a probability other than zero. But it is important that the cooling is sufficiently slow so that the solid reaches thermal equilibrium at each stage. If not, defects can be frozen into the solid and it does not reach the minimum energy state. Finding a minimum-energy state of a solid is an optimization problem, and not that different from many problems we come across in combinatorial optimization.

With simulated annealing the solutions $i \in S$ of the combinatorial optimization problem can be seen as states of a physical system. The cost function f is then the equivalent of the energy E_i of the system in the state i. The particles arranging themselves at a certain temperature T is the same as perturbing the system from state i to state $j \in N(i)$. We see that T is just a control parameter, and this can be varied over time. Simulated annealing can be seen as applying the criterion,

$$P[accept\ j] = \begin{cases} 1 & E_j \leq E_i \\ e^{(E_i - E_j)/T} & E_j > E_i \end{cases} \tag{5.2}$$

at the different temperature levels. At each level, the system is given enough time to reach a steady state. As opposed to iterative improvement, the probabilistic behavior of simulated annealing gives the algorithm a chance to escape local minima. Simulated annealing has been put on firmer ground in recent years after being modeled as a finite Markov chain. It is shown in [39] that the algorithm does converge to the global minimum given a few constraints. The cooling schedule, explained below, must satisfy

$$\lim_{k \to \infty} T_k = 0 \quad and \quad T_k \geq T_{k+1} \tag{5.3}$$

Secondly either T_k must go through an infinite number of transitions or T_k must not tend to zero faster than $1/\ln(k)$. If these restrictions are not satisfied the algorithm no

longer guarantees an optimal solution. In applications, one rarely has any way of knowing if the solution is optimal or not.

5.2.2. Algorithm

To use the algorithm the followings are required:

- Describing all configurations of the system.
- Generating stochastic changes in the configuration of the system.
- Defining a cost function to each configuration where finding a minimum is desired.

Fortunately this applies to a wide range of optimization problems. We let *Temp* be the temperature function, and the function *P* perturbs a configuration into a neighboring configuration. Here rnd(0,1) denotes a stochastic variable uniformly distributed on the interval (0,1). The algorithm can then be written in pseudo-code as shown in Figure 5.1.

```
Initialize X₀ and T₀
for i = 1 to num_of_iter
        Tᵢ = Temp(Tᵢ−1)
        for j = 1 to num_of_pert
                Xp = P(Xⱼ₋₁)
                ΔE = E(Xp) − E(Xⱼ₋₁)
                if ΔE < 0 or e^(−ΔE/Ti) > rnd(0; 1)
                        Xⱼ = Xp
                else
                        Xⱼ = Xⱼ₋₁
                end
        end
end
```

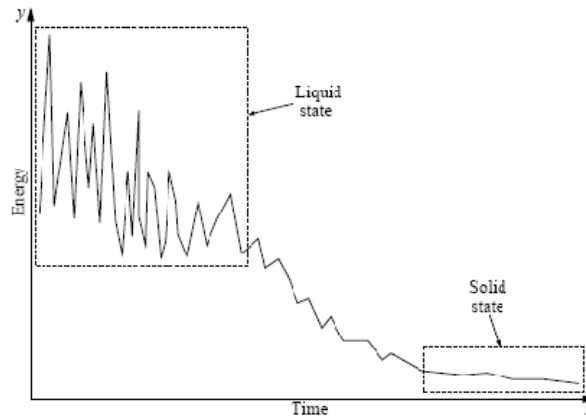Figure 5.1. Simulated annealing algorithm.

Figure 5.2. Energy level vs time.

We see here that the algorithm starts with an initial configuration X_0 and temperature T_0. At T_0 the system is "melted", and at $t_{num\_of\_iter}$ it is "frozen". At each temperature level the system is perturbed *num_of_pert* times to reach the steady state, and it goes through *num_of_iter* temperature levels.

5.2.3. Parameters

How the algorithm converges is strongly dependent on how the parameters are chosen. These change according to the problem, so the parameters should be chosen carefully. The best values are found through trial and failure. These parameters are:

- Those describing the development of the temperature, i.e. the initial value T_0, the end value $T_{num\_of\_iter}$ and the decrementation ΔTi. The parameters involving the temperature are also known as control parameters, as they control the probability that the algorithm accepts increases in the cost function.
- Those governing the neighboring configurations, i.e. the neighboring space and the number of perturbations per iteration *num_of_pert*.

When these parameters are specified they are referred to as the cooling schedule. If the cooling schedule is chosen carefully the energy-level compared to time will evolve somewhat like that of the plot in Figure 5.2.

In [40] a distinction is made between two types of cooling schedules, dynamic and static. In a dynamic cooling schedule the parameters are allowed to change as the algorithm progresses. With the static cooling schedules the parameters remain constant. Dynamic cooling schedules use information obtained during the running of the algorithm to update the parameters. However during the thesis small values were chosen for both *num_iter* and *num_pert*, so only static cooling schedules will be examined.

5.2.4. Initial Temperature

The initial value of the control parameter T_0 has great importance and should be chosen so that almost all perturbations are kept in the beginning, i.e. *P[ΔE] ≈1*. This is equivalent to the system being "melted".

A simple method for determining T_0 is proposed in [40]. Let ΔE_{max} be the biggest difference in cost between two neighboring configurations. We then choose

$$T_0 = \Delta E_{max} \qquad\qquad (5.4)$$

gives several ways of finding values for T_0 [39]. The first one, originally proposed by Kirkpatrick, uses the acceptance ratio. Let T_0 have a large value, and go through a given number of transitions. The acceptance ratio χ is then defined as the number of transitions accepted divided by the number of transitions. If this number is lower than a given value χ_0 (i. e. $\chi_0 = 0.8$) then the value of T_0 is doubled. This procedure is repeated until χ exceeds χ_0.

5.2.5. Final Temperature

We now look at the final value of the control parameter T. It must be chosen so that no more perturbations are accepted, i.e. *P[ΔE] ≈0*. An easy way to choose this is simply by following the strategy of Equation (5.1), but instead using the smallest change in the cost-function between two neighboring configurations as $T_{num\_of\_iter}$. That is, if ΔE_{min} is the smallest difference in cost between two neighboring configurations, we should choose

$$T_{num\_iter} = \Delta E_{max} \qquad (5.5)$$

This parameter controls how long the algorithm runs, and if the difference between neighboring configurations is small this gives a long running time.

5.2.6. Decrementation Rule

For the algorithm to terminate in the global minimum or near this it is important that it is cooled sufficiently slow. If not it can get "stuck" in a local minimum. Therefore it is necessary to use small decrements in the temperature, and that the algorithm is given enough time to become stable at each temperature. Van Laarhoven *et al.* [39] suggests several decrementation rules:

- Using the decrementation rule

$$T_{i+1} = \frac{\Gamma}{\ln\left(e^{\frac{\Gamma}{T_i}} + 1\right)} \qquad (5.7)$$

one is guaranteed convergence of the algorithm. But then there is the problem of determining the value for Γ. One conservative estimate could be $\Gamma = \Delta E_{max}$, but this results in a very slow convergence of the algorithm, and too slow for practical means for a problem of some size.

- A common decrementation rule is to let

$$T_i = c^i T_0, \quad i = 1,2,\dots\dots, \qquad 0 < c < 1 \qquad (5.8)$$

A practical value for c would then be between 0.8 and 0.99. [17] uses $c = 0.9$ for an electronic systems design problem.

- One decrementation rule is letting the temperature difference be constant,

$$T_i = \frac{num\_iter - 1}{num\_iter} T_0, \quad i = 1,2,3,\dots\dots \qquad (5.9)$$

- A slower decrementation rule is

$$T_i = \frac{T_0}{ci}, \qquad i = 1, 2, \dots \tag{5.10}$$

There is a trade-off in the algorithm between finding an optimal solution and reasonable computational time.

5.2.7. Neighboring Configurations

The number of neighboring configurations gives the stochastic freedom of the algorithm. Choosing a suitable neighborhood function is very problem dependent. For optimization of physical designs, which array optimization falls under, it is natural to define neighboring configurations by just the permutation of one element.

5.2.8. Number of Perturbations

The choice for the number of perturbations at each temperature level T_{num_pert} should in some way be related to the size of the problem. The size of the problem is best described by the stochastic freedom of the algorithm, i.e. the number of configurations. So we should have that

$$numpert \propto \binom{N}{K} \tag{5.11}$$

Chapter 6

Circular Ring Arrays

Circular ring arrays best fit on the front side of the catheter and is a preferred array system for IVUS. Due to their circular symmetry and spatial diversity on the coarray, they produce lower side lobes when compared with periodic rectangular arrays. Therefore, an element distance of larger than $\lambda/2$ can be considered. In addition, circular ring arrays also enable 3-D volumetric imaging by scanning a conical volume in front of the array plane. They can be designed in single or multiple ring structure. A schematic description of a FL-IVUS probe with circular ring arrays and monolithically integrated front-end electronics is shown in Figure 6.1.
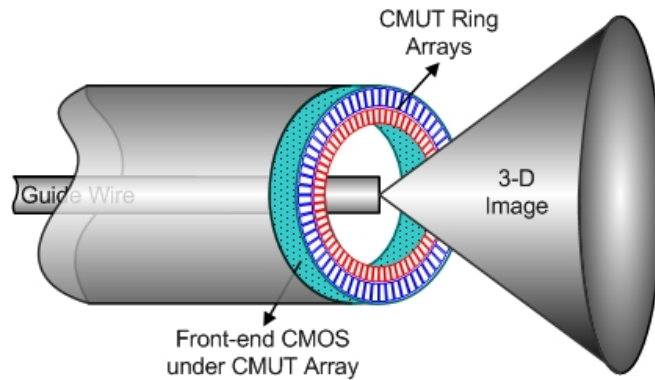
Figure 6.1. Schematic of a FL- IVUS probe with circular ring arrays and monolithically integrated front-end electronics.

Single ring arrays are formed by coaxial array of elements located around the probe in an equally spaced circumferential manner. The array elements are both used in transmit and receive operation. The viability of FL-IVUS imaging using a single ring array has been demonstrated by several studies in literature. Recently it was proposed in [50, 54] that a CMUT based array configuration consisting of two circular rings

(dual rings) with separate transmit and receive functionality which is a particular case of multiple ring array configurations. The main advantage of dual ring array configuration is eliminating the Tx/Rx switching circuitry. Moreover, dual ring configuration provides identical resolution without losing active area when compared to single ring array.

The theoretical far field continuous wave two way PSF of a dual ring array is given by:

$$P(r) = J_0(kar/z) \cdot J_0(kbr/z) \qquad (6.1)$$

where $J_0(.)$ is the zero-order Bessel function, $k=2\pi/\lambda$, λ is wavelength, z is range, r is a radial coordinate, a and b are radius of transmit and receive arrays. Similarly, the PSF of single ring array can be determined by defining the radii of transmit and receive arrays as equal. These circular ring array responses have high level side lobes when compared with the full disk aperture which has a PSF of the form J_1 which represents the first order Bessel function.

Optimizing an array will not only reduce side lobe level but also reduce the number of firings which produce high frame rate and minimize motion artifacts. As the optimization problem is complex, analytical methods are not used in designing optimized arrays. Synthesizing ring arrays is more cumbersome due to the circular geometry when compared with the 2-D rectangular arrays. Therefore, this forces us to use coarray concept to simplify the 2-D optimization problem by reducing to 1-D. The objective of the optimization is to obtain a predefined number of optimal firing set which results in an elimination of redundant spatial frequencies in the coarray and furthermore producing low side lobe PSFs.

6.1. Coarray Approach

In array design, the coarray concept can be used as a guiding tool for synthesizing appropriate transmit and receive array configurations. The coarray corresponds to the convolution of Tx and Rx arrays and represents the two-way aperture function, equivalently the spatial frequency response. Each Tx-Rx element pair contributes to

a specific bin of the coarray, representing a specific lateral spatial frequency. The location of the bin corresponds to the sum of the position vectors of the Tx and Rx elements. The overall coarray kernel extends to the sum of the sizes of Tx and Rx apertures. The goal in array design is to form a uniform coarray function, where amplitude of each coarray element must be controllable by adjusting the Tx and Rx element apodization weights.
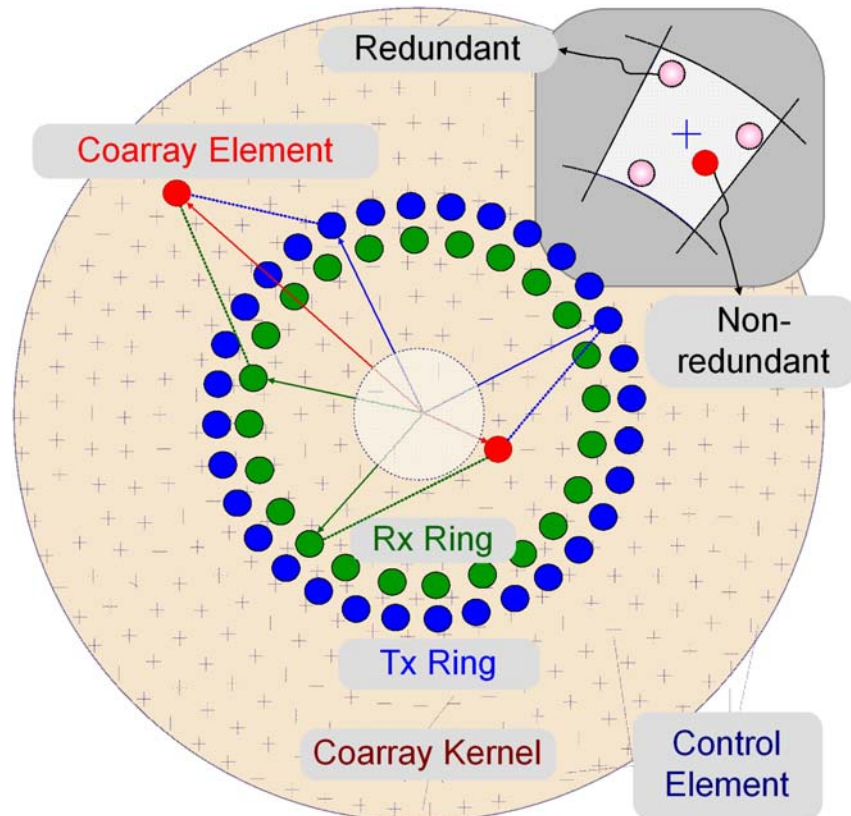
Figure 6.2. Schematic representation of coarray formation of dual-ring. Choosing the non- redundant elements is demonstrated at the upper right portion of the coarray.

The coarray kernel for ring arrays fills a circular area with a boundary radius of $R_{tr}+R_{rc}$ (R_{max}), where R_{tr} and R_{rc} represent the radius of transmit and receive ring arrays respectively. The full set of all Tx-Rx combinations produces too many spatial frequencies (firings) since it has $N_{tr} \times N_{rc}$ elements. Since the number of firings must be minimized for real time imaging in IVUS, the goal is to form a coarray function, where the beam pattern has lower side lobe level. In general, a suitable weighting function is used to suppress the side lobes in beam patterns but this method

compromises SNR which is very important for IVUS applications. Therefore, we propose two sampling strategies to obtain reduced sets based on the idea of adjusting the element density of the coarray rings in radial and angular directions to suppress side lobes.

6.2. Uniform Coarray Sampling

The spatial frequency components near the center of the coarray kernel corresponds to a spatial DC and has no contribution in image quality [41]. Therefore, a central hole in coarray kernel with a radius of R_{min} is determined and removed which forms a donut shape. To form a uniformly sampled control kernel, the coarray space between R_{min} and R_{max} is sampled at equal radial and equal angular distances to obtain a desired number (N_d) of firings (coarray elements). Each sample is the center of an equal area patch shown in Figure 6.2. To obtain a uniform distribution, we choose the nearest neighbor elements to the control coarray elements from the full-set coarray elements. Other elements apart from this nearest element are discarded. Using this approach, we chose a subset of N_d elements from the full set to obtain a non-redundant coarray subset companion with the uniformly sampled control kernel, and determine the corresponding Tx-Rx pairs.

6.3. Non-Uniform Coarray Sampling

Although the non-redundant set is similar with the uniformly sampled control kernel, it has some disparity distributed over all of the non-redundant set elements that reduces periodicity on coarray pattern and hence results in a reduction in grating lobe level. To fully eliminate the periodicity we used a non-uniform coarray sampling method. In this method, the coarray kernel is sampled to adjust the element density distributed in a decreasing manner from inner ring to outer ring by increasing radially inter-element distance of the rings to fit a given apodization function. This method not only helps suppressing grating lobes but primarily aims to reduce side lobes. The procedure in obtaining the non-redundant coarray subset is the same as uniform coarray sampling approach.

6.4. Simulated Annealing Optimization

Sampling coarray technique both in uniform and non-uniform fashion gives completely heuristic solutions to the optimization problem. To obtain a coarray pattern with a desired PSF performance one should search the entire N_d element subsets of the full set coarray. These problems cannot be solved by polynomial time as they are non-deterministic polynomial time (NP-complete) problems. Therefore algorithms that can find near optimal solutions in reasonable time have received a lot of attention. For this purpose simulated annealing algorithm is proposed in this thesis.

The simulated annealing algorithm was first introduced by Kirkpatric [36] and widely used in array optimization, circuit design and image processing. It mimics the behavior of the molecules of a pure substance during the slow cooling that results in the formation of a perfect crystal. The use of this technique to solve other types of problems is based on the analogy between the state of each molecule and the state of the set of parameters that affects the performance of the system to be optimized. An energy (cost) function is defined for the system, which reduces with improved performance of the system. The algorithm is iterative. At each iteration, a small random perturbation is induced in the state. If the new state causes the energy function to reduce, it is accepted. Otherwise the state is accepted with a probability dependent on the temperature of the system, in accordance with the Boltzmann distribution given as,

$$p(\Delta E) = e^{-\frac{\Delta E}{kT}} \tag{6.2}$$

where k is the Boltzmann constant and T is the temperature of the system. The temperature T is gradually lowered by a temperature function of the iteration number. As the system cools off, the probability for accepting a poor solution is reduced, and eventually the system converges on the final solution which, if the optimization parameters are chosen well, may be close to the optimal solution.

To implement the algorithm to the problem, we first calculated the PSF $H(.)$ for a point target based on the Rayleigh-Sommerfeld diffraction formula using the following expression[26]

$$H(r,\theta,\varphi) = \sum_i w_i \cdot \sum_j w_j \cdot s(\frac{2r}{c} - t_i - t_j - \tau_i - \tau_j) \qquad (6.3)$$

where (r,θ,φ) are the spherical coordinates, i and j represent the transmit and receive indices respectively, $s(.)$ is the excitation pulse, c is the speed of sound, t_i and t_j are the flight times between the point target and transmit and receive elements respectively, τ_i and τ_j are the corresponding focusing delay times. The term $w_{i,j}$ represents the weighting coefficients. In our design we used uniform weighting which means no apodization and hence they are both equal to unity. To avoid computational complexity, we ignored the element factor, obliquity factor and the attenuation effects. The PSF geometry showing the array and spherical coordinate system is shown in Figure 6.3.

The initial step for the optimization algorithm is to calculate the PSF including all the Tx-Rx firing combinations for all the sampled azimuth and elevation angles. This data is recorded to be further used in the iterations to prevent repeating PSF calculations for each perturbation state and enable a large amount of reduction in computational time. To find an optimum solution set from the full set coarray with a desired number of elements, one can define an energy function $f(X_i)$, where X_i is the coarray element position vector. To minimize the side lobe level the energy function should be defined as,

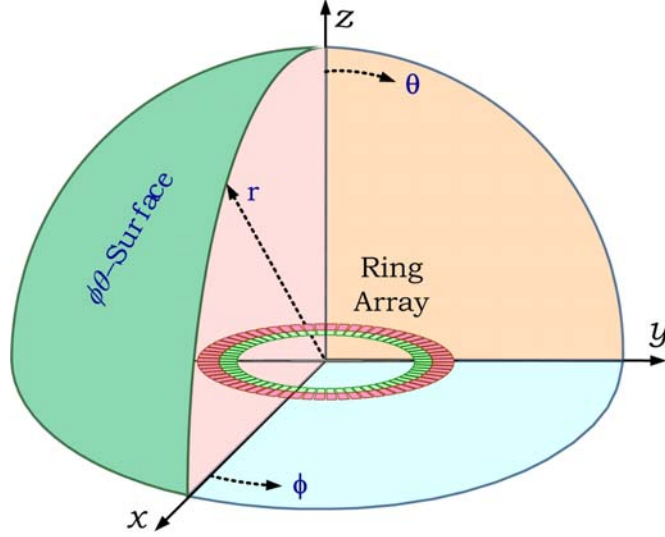$$f(X_i) = \max_{\theta \geq \theta_i} |H(r,\theta,\varphi)|^2 \qquad (6.4)$$

Figure 6.3. Reference geometry used for simulated PSFs

where θ_i is the angle of main lobe to side lobe transition.

The objective of the optimization is to minimize the energy function in terms of peak side lobe level. Another energy function can be defined to minimize the integrated side lobe energy. The expression is given as,

$$f(X_i) = \int\limits_{\theta_i}^{\frac{\pi}{2}} \int\limits_{-\frac{\pi}{2}}^{\frac{\pi}{2}} |H(r,\theta,\varphi)|^2 \, d\varphi d\theta \qquad (6.5)$$

Due to the symmetric array geometry, the PSF is also symmetric. Therefore, considering the spherical coordinate angles of ($0 \leq \theta \leq \pi/2$, $-\pi/2 \leq \varphi \leq \pi/2$) is sufficient to represent the PSF characteristic and achieve a reduction in computation time.

The optimization procedure is started after determining suitable temperature function and number of iteration and perturbation parameters. To determine the parameters one should also be concerned about the chosen energy function. The initial temperature is chosen high enough so that the first perturbations are almost always be accepted which result in sharp variations on the energy function. A randomly chosen element set from the full set determines the initial energy state value and after that the iterations start. In every iteration, a predetermined number of perturbations

47

on the current subset vector is performed. In every perturbation, a randomly chosen single element replaces with a randomly chosen non-used element. If this new state decreases the energy function it is accepted, if not it is accepted with the defined probability function. The new state (element set) is updated if it is decided to be accepted. This procedure is performed till all the predefined number iterations and perturbations are completed. At the end of the procedure, the variations on the energy function are reasonably decreased which yields an optimal element set. The flow chart of the optimization procedure is shown in Figure 6.4.
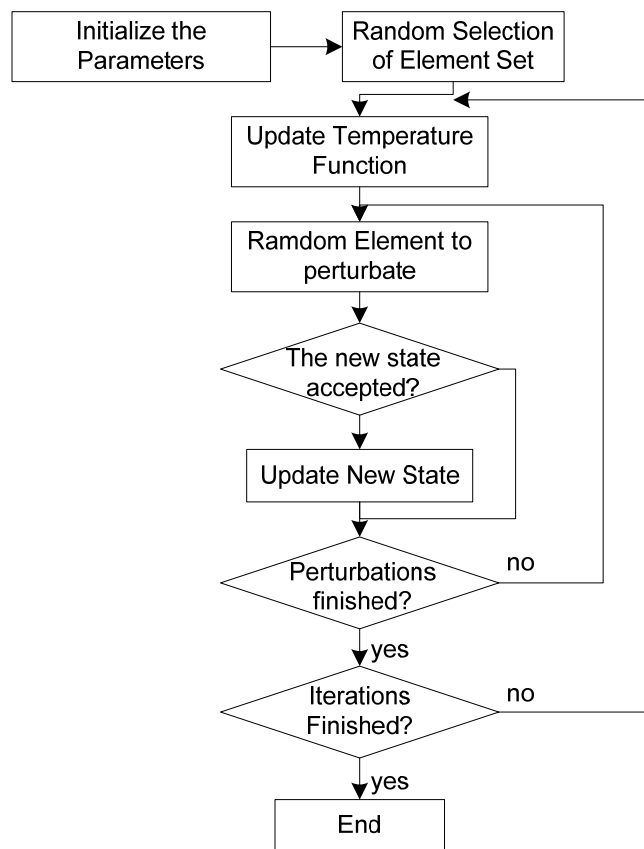
Figure 6.4. Flow-chart of the optimization procedure.

6.5. Simulation Results

To test the imaging performances of the optimized array configurations with dual and single ring arrays, we performed custom numerical simulations. For test arrays we consider a single array with 64 Tx elements and a dual ring array of 64 Tx and 58

Rx elements. The diameter of the single ring array is 1200 μm whereas the diameters of the Tx and Rx arrays of the dual-ring array are 1200 μm and 1080 μm, respectively.

To analyze the coarray patterns we first obtained the full set coarray of the corresponding array configurations. The full set has 3712 and 4096 firing combinations for dual and single ring arrays respectively. Due to different Tx and Rx array radii and number of array elements, all the firing combinations have uniform amplitude, in other words there is no overlap in the coarray space. However, same Tx-Rx pairs form an identical point on the coarray space and hence single ring array has some redundancy. When we eliminate this redundancy, we may consider 2049 firing elements that have uniform amplitude.

For dual ring array configuration we define a number of desired element set for two test cases of 512 and 256. These desired element sets result in a reduction of nearly 1/7 and 1/14 of the full set. 256-element coarray set is chosen especially to test the real time imaging performance. To compare coarray distributions we obtained uniform and non-uniform sampled coarrays as well as the optimized coarray. For uniformly sampled coarray we determined 13 rings and 9 rings with inter-element distance of nearly 1.2λ and 1.7λ for 512 and 256 element designs respectively. For non-uniformly sampled coarray we used Kaiser-Bessel apodization function to fit the radial inter-element distance. The Kaiser-Bessel function is expressed as,

$$\Delta r(i) = \frac{I_o(\alpha\sqrt{1 - \left(\frac{2i}{N} - 1\right)^2})}{I_0(\alpha)} \tag{6.6}$$

where Δr is the inter-element distance of rings, i is the ring index, I_0 is the zero-order modified Bessel function of the first kind, α is an arbitrary parameter and N is the total number of rings. To obtain a desired element number of 512, we determined a minimum and maximum inter-element distance of 0.8λ and 1.34λ, respectively, whereas for 256-element case these numbers are 1.2λ and 2.0λ respectively. The number of rings are identical with the uniformly sampled case. For both uniform and non-uniform sampled cases coarrays subsets are determined by nearest neighbor technique. We used the parameters: 400 iterations, 4000 perturbations and the initial

temperature value of 3.10^4 to obtain the optimized set. For the temperature function we used,

$$T(i) = T_0 \beta^i \qquad (6.7)$$

where T_0 is the initial temperature, i is the iteration index and β is a parameter chosen as 0.97. We performed the simulations with energy functions using both minimizing the peak side lobe and the integrated side lobe energy techniques. Although they produce similar results, the former yields better results than the latter. To obtain a circularly symmetric coarray and PSF distribution, when choosing elements we used a quarter of the coarray space and extended the solution to the other quarters symmetrically. This also results in a symmetric Tx-Rx firing pairs. Another advantage of this method is that the optimization is performed on a small search space which reduces computational time to reach an optimum solution. The coarrays produced by all the Tx-Rx element pairs (full-set), uniform sampled, non-uniform sampled and optimized cases are shown in Figures 6.5- 6.7 (top row). In these figures, the coarray elements are represented as point and display consists of binary values, i.e., 0 (black) and 1 (white).

For the wide-band PSF simulations of dual ring array we used a gaussian pulse with a center frequency of 20 Mhz. The speed of sound is equal to 1540 m/s and the sampling frequency is 2 GHz. The fractional bandwidth is chosen as 50% and 80%. For displaying 2-D PSFs, we used constant-r surface ($\theta\varphi$-surface) and a $r\theta$-plane (in spherical coordinates as depicted in Figure 6.3), which correspond to the C-scan and B-scan displays, respectively. Each image in these figures was normalized to its own maximum and log compressed to 40 dB dynamic range. Here the target is located on the array normal (on axis) at *f/4*, and hence these PSFs represent non-steered beam patterns. The C-scan and B-scan images are shown in Figures 6.5-6.7 (middle, bottom). For ease of comparison, we also obtained averaged 1-D lateral cross-sections of the PSFs shown in Figures 6.5-6.7, where the averaging was performed by the 1-D cross-sections across the entire φ-range and the r-range, respectively.

When the 2-D PSF responses of dual ring array are examined, we observe that optimized coarray configuration has narrow -6dB main lobe width when compared

with uniform and non-uniform sampled cases. For the first side lobe the non-uniform sampled coarray, as expected, has lower than the uniform sampled coarray. On the other hand, optimized coarray produces considerably better performance than the other two. Although the average side lobe level of uniform and non-uniform sampled coarrays decrease under -40dB level around 10° angle, a relative rise to the -35dB in the far side lobe region can be observed. For the optimized coarrays both in 512 and 256 element cases, there is a slightly flat side lobe level near -40dB. Especially in 512-element case the far side lobe level for optimized coarray remains under -40dB almost every angle. We have also simulated PSFs for FBW of 80% for both 512 and 256 element sets. The results for 512-element case is shown in Figure 6.7. The optimized coarray produces the best results as it was seen in the results for FBW of 50% case. The main difference in FBW of 80% is on the non-uniform coarray case where there is a widening beneath the main lobe region and a rise on the far side level. This is consistent because as the FBW is increased, large inter-element distances on outer rings of the coarray results in a rise in side lobe region. The measurements on simulation results in terms of beam width, peak first side lobe level and far side lobe levels are outlined in Table 6.1.
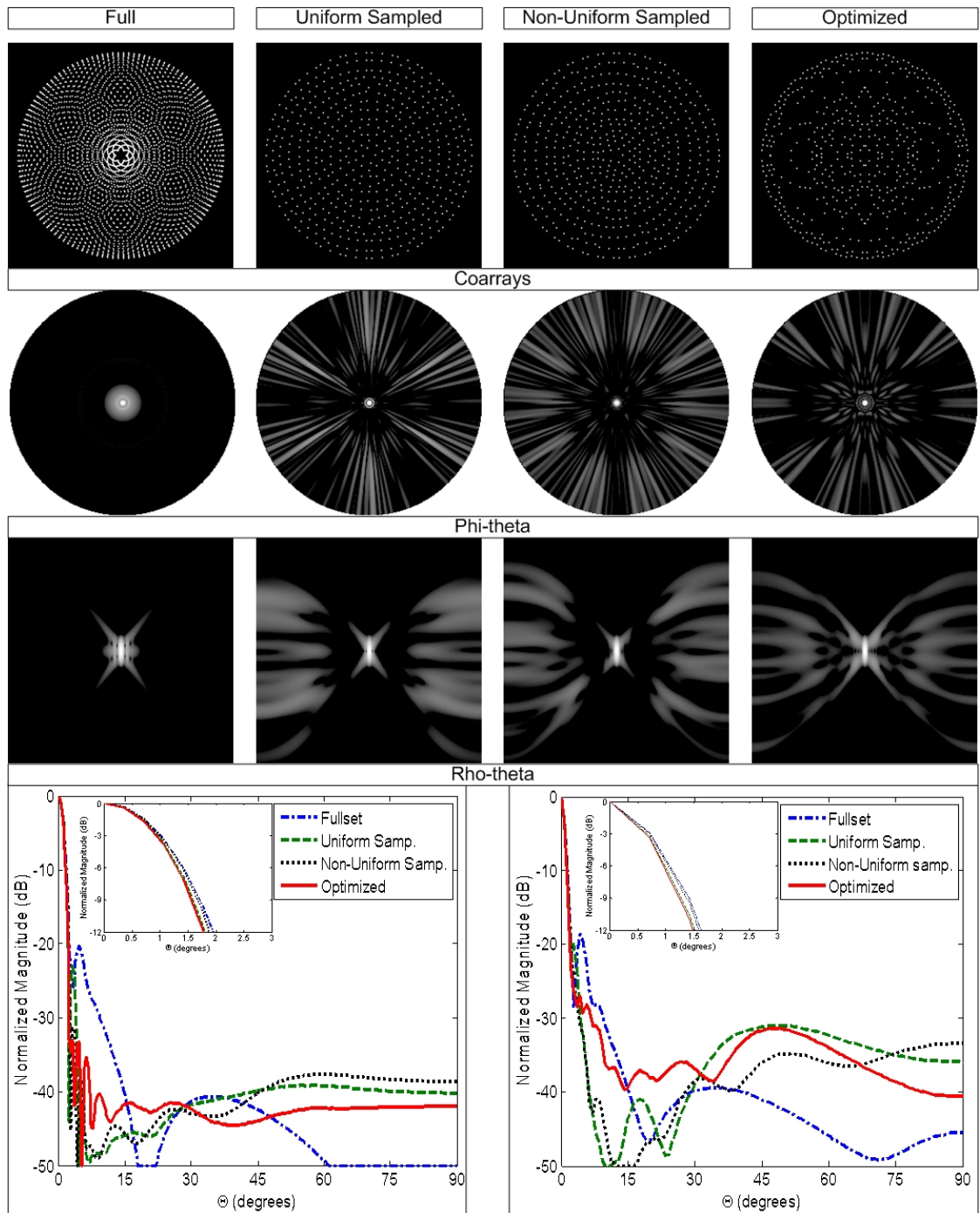
Figure 6.5. Simulation results for 512-element coarray of dual ring array (FBW 50%).
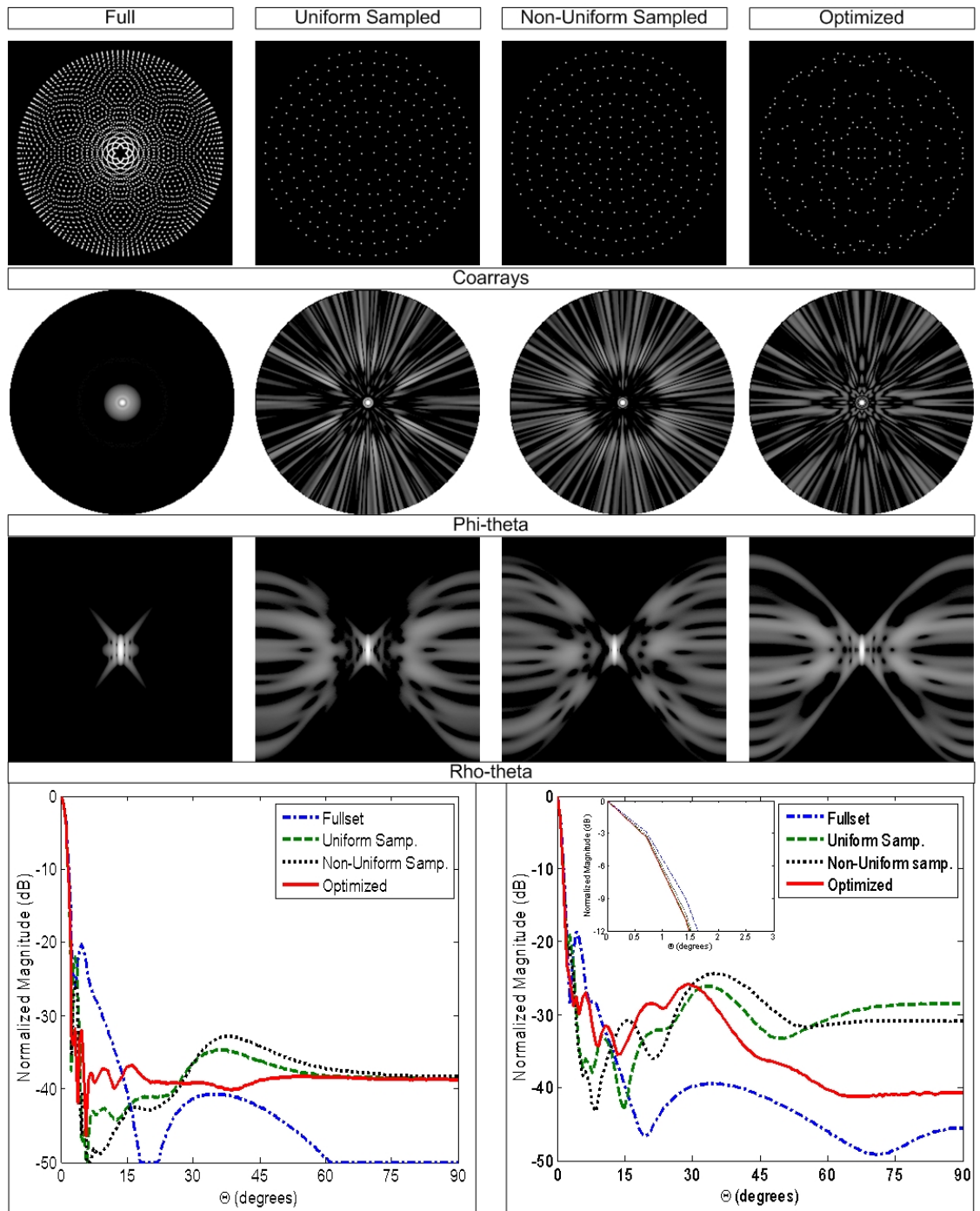
Figure 6.6. Simulation results for 256-element coarray of dual ring array (FBW 50%).

For the PSF simulations of single ring array we used a gaussian pulse with a center frequency of 10 Mhz which is the value that Wang *et al.* [41] used in their study. The coarrays produced by all the Tx-Rx element pairs (full-set), non-uniform sampled and optimized coarrays are shown in Figure 6.8 (top row). A comparison for single ring array design, the coarray for Wang's approach is also given as a reference. We also produced 2-D PSFs of the corresponding coarrays and for comparison we plotted 1-D averaged cross-sections (Figure 6.8). The simulation results showed that the optimized and non-uniform sampled coarray has narrower -6dB main lobe width. Wang's coarray and non-uniform sampled coarray perform similar in terms of first and far side lobe level, while the optimized design has nearly 8dB improvement for the first side lobe level.

For single ring arrays Wang *et al.* [41] have presented results on coarray formation using a reduced set of Tx-Rx element pairs. Their approach in choosing the reduced set was based on predefined spatial offsets between the Tx and Rx elements' locations (i.e., indexes). This approach has also been used by Yeh *et al.* [42] for forward-looking intravascular/intracardiac imaging using a single-ring CMUT array. It seems that Wang's and our approaches produce coarrays with different sampling configurations of the coarray kernel: the former involves non-uniform sampling with density decreasing as the distance from the coarray center increases, whereas the latter produces nearly uniform sampling and non-uniformly distributed coarray elements density to fit an apodization function. These two coarray formation approaches for single-ring arrays can yield similar image quality, as long as the coarray size and the number of Tx-Rx pairs are identical. Because of the limitation in finding a proper set of offsets between the elements of the concentric rings with different element counts, the coarray synthesis using predefined offsets is not suitable for the dual-ring or multiple-ring array configurations, where each ring has a different number of array elements and/or inter-element separation. Therefore we used simulated annealing algorithm to obtain optimal coarray sets in both dual ring and single array designs. The optimized set for single ring array produce considerably better results than other coarray sampling approaches.
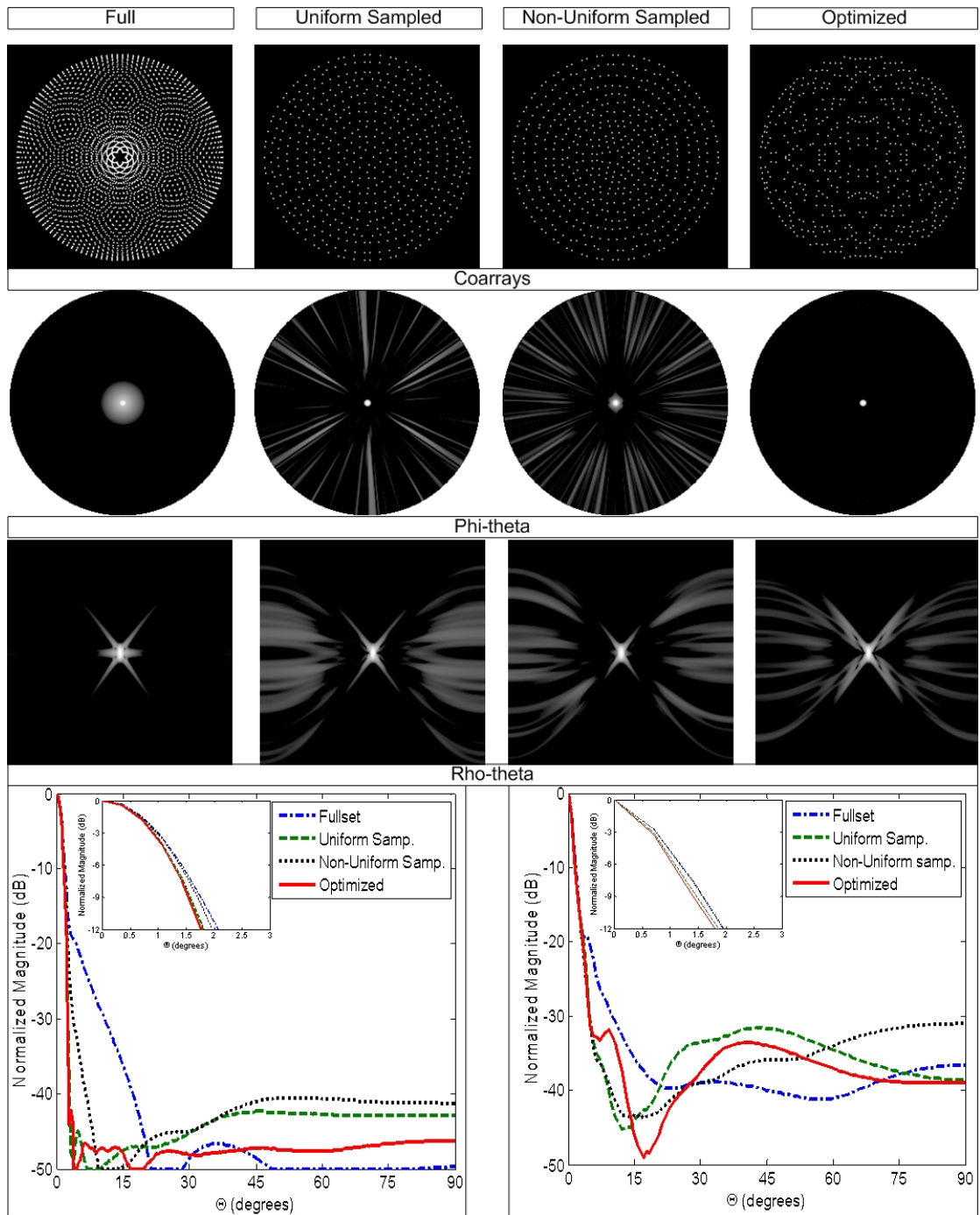
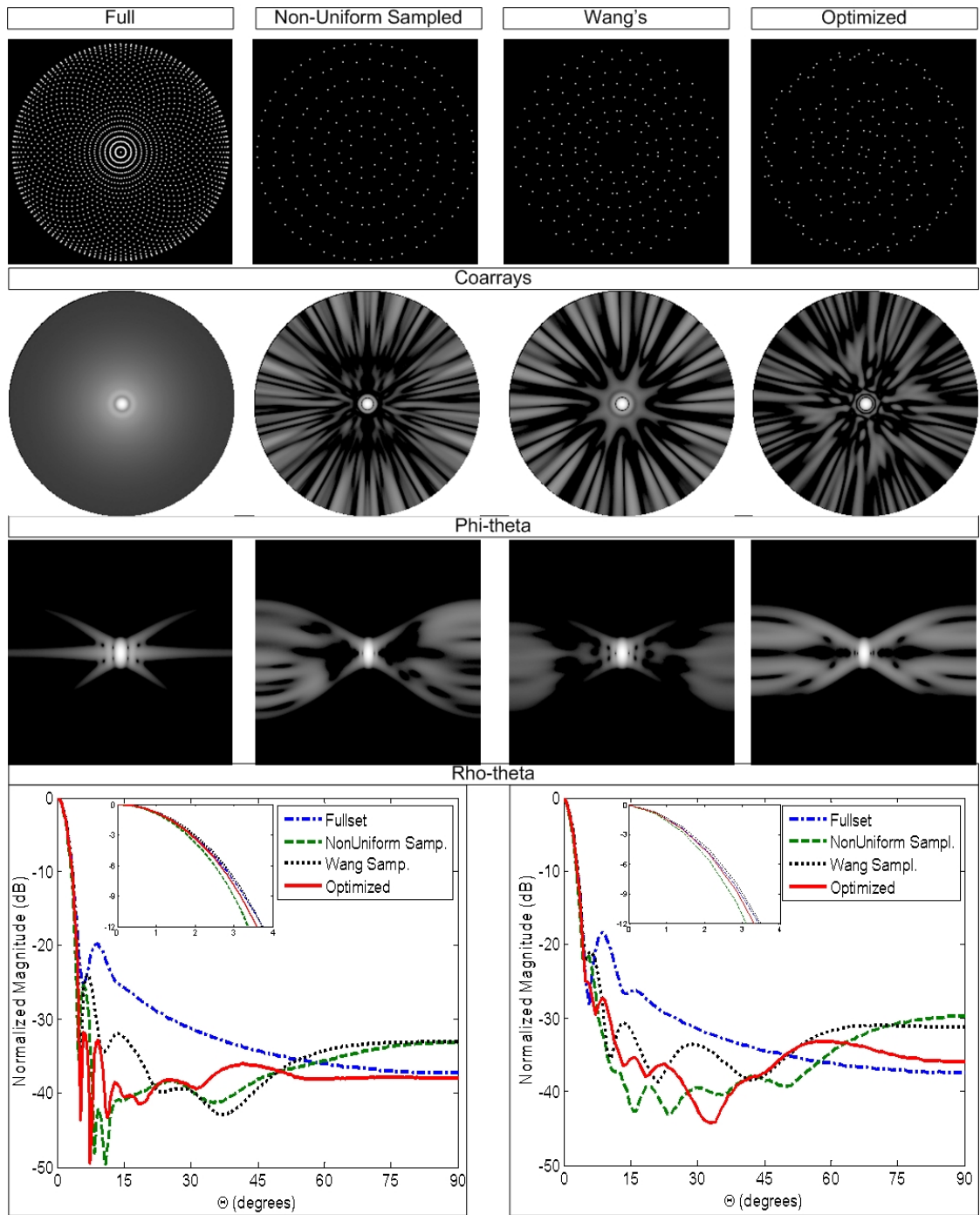Figure 6.7. Simulation results for 512-element coarray of dual ring array (FBW 80%).

Figure 6.8. Simulation results for 210-element coarray of single ring array.

6.6. Discussion

We present different optimized array designs based on dual and circular rings that are suitable for synthetic phased array processing with reduced number of firings. The designs are based on coarray concept. To obtain optimal firing set that produces low side lobes in the coarray we used simulated annealing algorithm by taking the wideband response of the array system as the energy function. The simulation results show that simulated annealing algorithm can be used to reduce the number of firings and control side lobe performance for circular ring arrays. Uniform and non-uniform coarray sampling strategies produced comparable results for all the test array designs.

For dual ring array design, we explored the coarray and imaging performance of two test cases with 512 and 256 firing elements. They both produced near side lobe level below -30 dB and far side lobe level of nearly -40 dB without compromising main lobe width. For 20 MHz operating frequency and 1 cm penetration, 256 firings configuration form an image frame in 3.3ms which yields nearly 300 frames/sec. When we consider only one channel is active during transmission and reception, 300 frames result in only 15 volumetric beam angles for 20 frames/sec. Parallel channels can also enable 3-D real time imaging with acceptable imaging performance for FL-IVUS.

Table 6.1. Simulation measurements on C-scan images.

	-6dB Beamwidth (°)	First Side Lobe Level (dB)	Far Side Lobe Level (dB)
	Dual Ring 512-Element (BW 50%)		
Full set	2.84	-20	<-40
Uniformly Sampl.	2.66	-23	<-38
Non-uniformly Sampl.	2.78	-31	<-38
Optimized	2.58	-34	<-42
	Dual Ring 256-Element (BW 50%)		
Full set	2.82	-20	<-41
Uniformly Sampl.	2.66	-22	<-35
Non-uniformly Sampl.	2.58	-25	<-34
Optimized	2.59	-32	<-39
	Dual Ring 512-Element (BW 80%)		
Full set	2.84	-20	<-47
Uniformly Sampl.	2.58	-45	<-42
Non-uniformly Sampl.	2.78	-30	<-40
Optimized	2.52	-43	<-47

Chapter 7

Hexagonal Ring Arrays

7.1. Motivation

As explained in previous sections, FL-IVUS and ICE imaging need catheter based ring shaped array systems. Circular ring arrays are widely used and studied due to their preferable geometry that can be placed around the guide wire. The distribution of coarray functions for both single and dual ring arrays produce non-uniformity due to their circular geometry. In array design the goal is to form a uniform coarray function, where amplitude of each coarray element must be controllable by adjusting Tx and Rx element apodization weights.

Another important challenge in FL-IVUS systems is low SNR due to the small array element sizes. 3-D real time imaging needs synthetic phased array which causes image SNR decrease when compared with conventional phased array. To eliminate this drawback and increase SNR, one needs large array elements on transmit to emit more ultrasound power to the imaging space.

To bring a solution to these problems, a new array architecture is proposed in this thesis which has an array structure of dual hexagonal rings. The proposed architecture is composed of independent Tx and Rx arrays which has sparse and large Tx array elements with hexagonal shaped small Rx sub-arrays. By using the advantage of CMUT technology, we can design arbitrary shaped array elements and this enables us to use hexagonal shaped elements in array design.

The motivation of using hexagonal structure in array design is that the optimal filling of a circular space can only be achieved by hexagonal geometry. In addition to this, the inter-element distance of array elements and, as a result, the coarray elements can give interesting flexibility to the optimization of PSF performance and beamforming

electronics. Another advantage of the structure is that a parameter independent configuration can be established for different array sizes and operating circumstances.
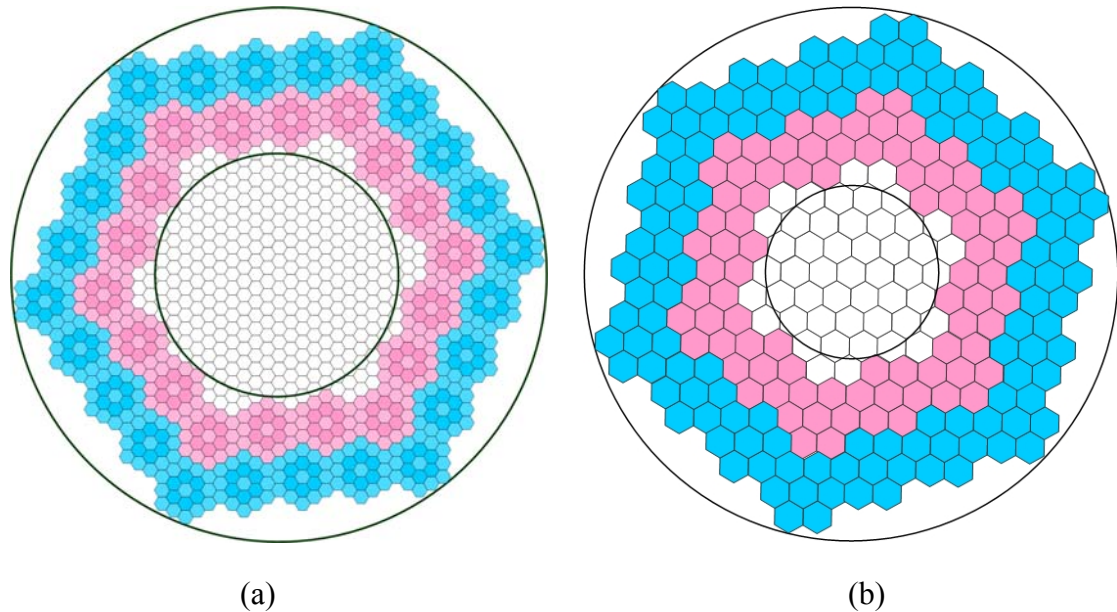

<p style="text-align:center">(a)   (b)</p>

Figure 7.1. Schematic description of forming dual hexagonal arrays for (a) 19-subarray and (b) 7-subarray elements.

7.2. Coarray Comparison

The schematic representation of dual hexagonal ring array structure is shown in Figure 7.1. It can be seen that two different array structure can be formed using dual hexagonal array. The circular area is fully populated with small hexagonal cells starting from center to the edge. The inclination on the array axis results from the nature of fully populated hexagonal sampling. According to the application and size of the catheter, these small cells are combined as a 7 or 19 element subarrays. The corresponding subarrays that compose a continuous ring shaped structure form Rx array. The array encloses the Rx array with same array element size forms the Tx array. To increase SNR on transmit operation the Tx array elements are formed as an electronically defocused annular array instead of hexagonal subarrays. This approach employes a large single element and improves image performance as well as SNR.

The hexagonal sampling and choosing neighbor elements as transmit and receive of dual hexagonal array structure yields a uniform coarray function as shown in Figure 7.2. On the top row of Figure 7.2, the Tx and Rx array structures of fully sampled hexagon array and dual hexagonal ring array are given. The bottom row shows the corresponding coarray functions. The middle column shows the full transmit and receive combination of the coarray where the right column shows the coarray function with the redundant amplitude distribution on the full coarray eliminated. The cavity or zero amplitude coarray space at the center is expected due to slightly different radial distance of Tx and Rx rings.
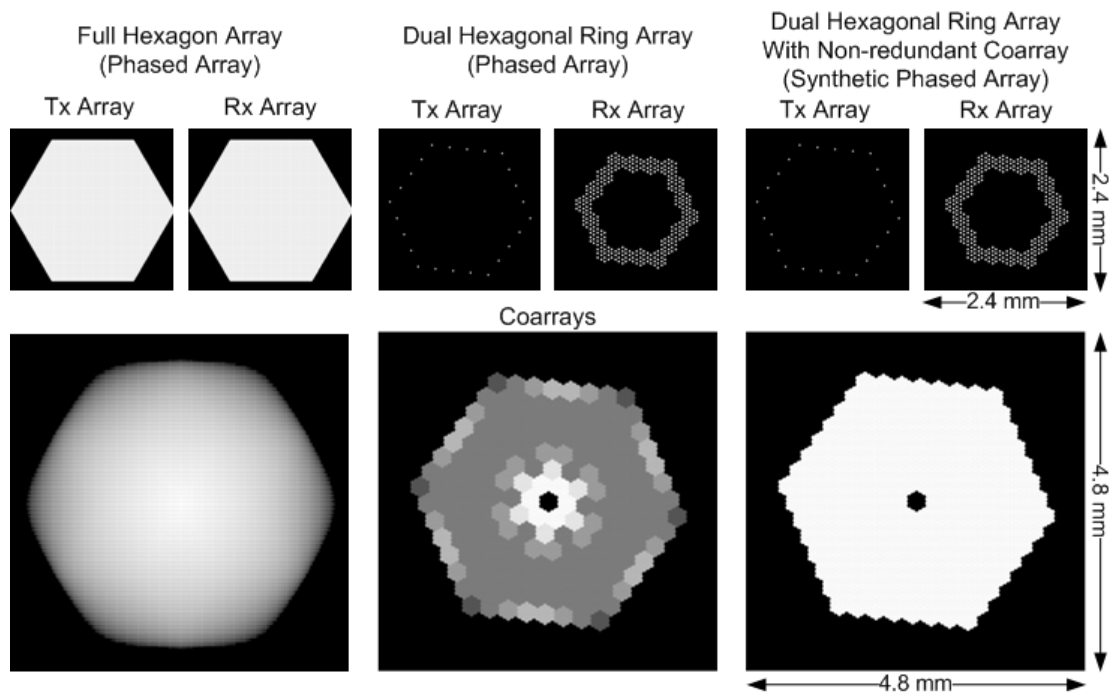

Figure 7.2. Tx-Rx array structures and corresponding coarrays for full hexagon, dual hexagon and dual hexagon with non-redundant coarray.
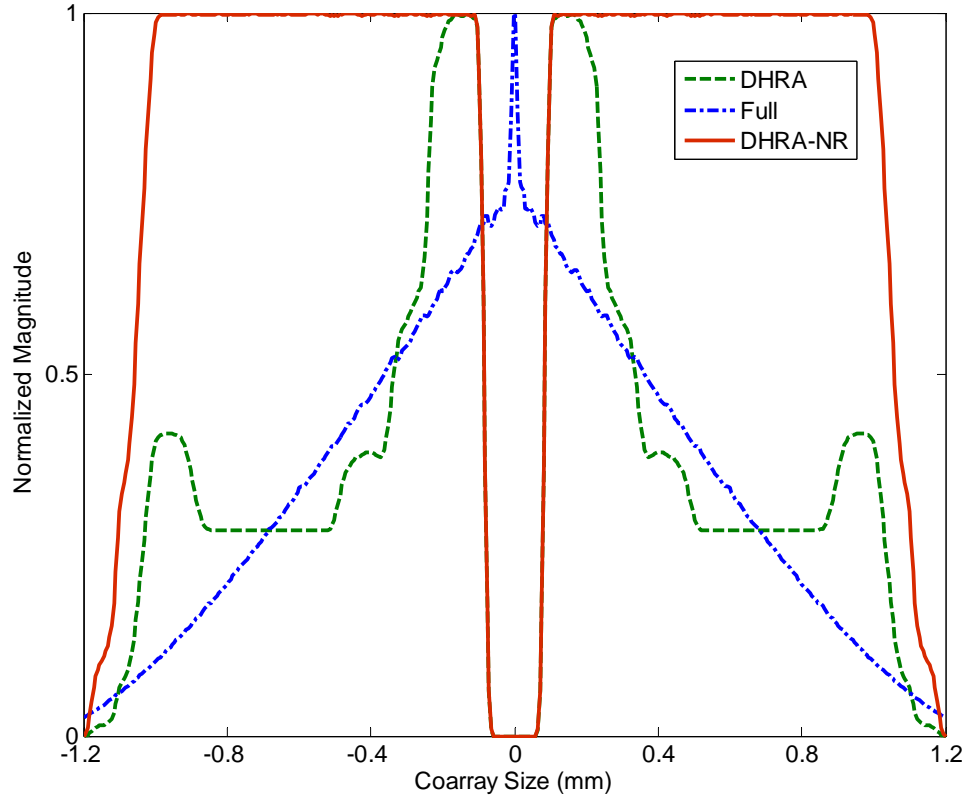
Figure 7.3. 1-D coarray comparison of full hexagonal (Full), dual hexagonal (DHRA) and dual hexagonal with non-redundant (DHRA-NR) coarray.

For ease of comparison we obtained 1-D cross-sections of the coarray functions which are shown in Figure 7.3. The non-uniformity on coarray functions for full hexagon and dual hexagonal ring with full Tx-Rx can be easily seen in the figure.

7.3. Design

Two different dual hexagonal array structure were designed. The first one is for ICE application. It is suitable for catheters larger than 2.4 mm diameter. The operating frequency is determined as 10 MHz which is suitable for ICE imaging. The Rx elements are composed of 18 elements with 19 subarrays. However, the Tx arrays are formed by 24 large defocused annular arrays with a diameter of 250 μm. The annular array has 7 rings with a ring width of 14 μm. This array configuration has a central circular cavity of nearly 1 mm diameter which is sufficient for the guide wire.

The second array structure is for IVUS application which has a 1.2 mm diameter. The central hole diameter in this case is 540 μm. The Rx elements are formed by 7-

element subarrays which is totally 126 elements. The number of Tx elements is 24 with defocused annular array diameter of 114 μm. Each annular array is formed by 5 rings with a ring width of 10 μm. The schematic representations of dual hexagonal ring array architectures for ICE and IVUS applications are shown in Figure 7.4.

Dual Hexagonal Ring Array

Tx Annular Subarray
(Defocused)

250 μm

Number of Rings = 7
Ring Width = 14 μm

1045um

1080um

784um

2400 μm

Rx Subarray

275 μm

60 μm

(a)

Dual Hexagonal Ring Array

Tx Annular Subarray
(Defocused)

114 μm

Number of Rings = 5
Ring Width = 10 μm

520um

540 μm

390um

1170 μm

Rx Subarray

140 μm

50 μm

(b)
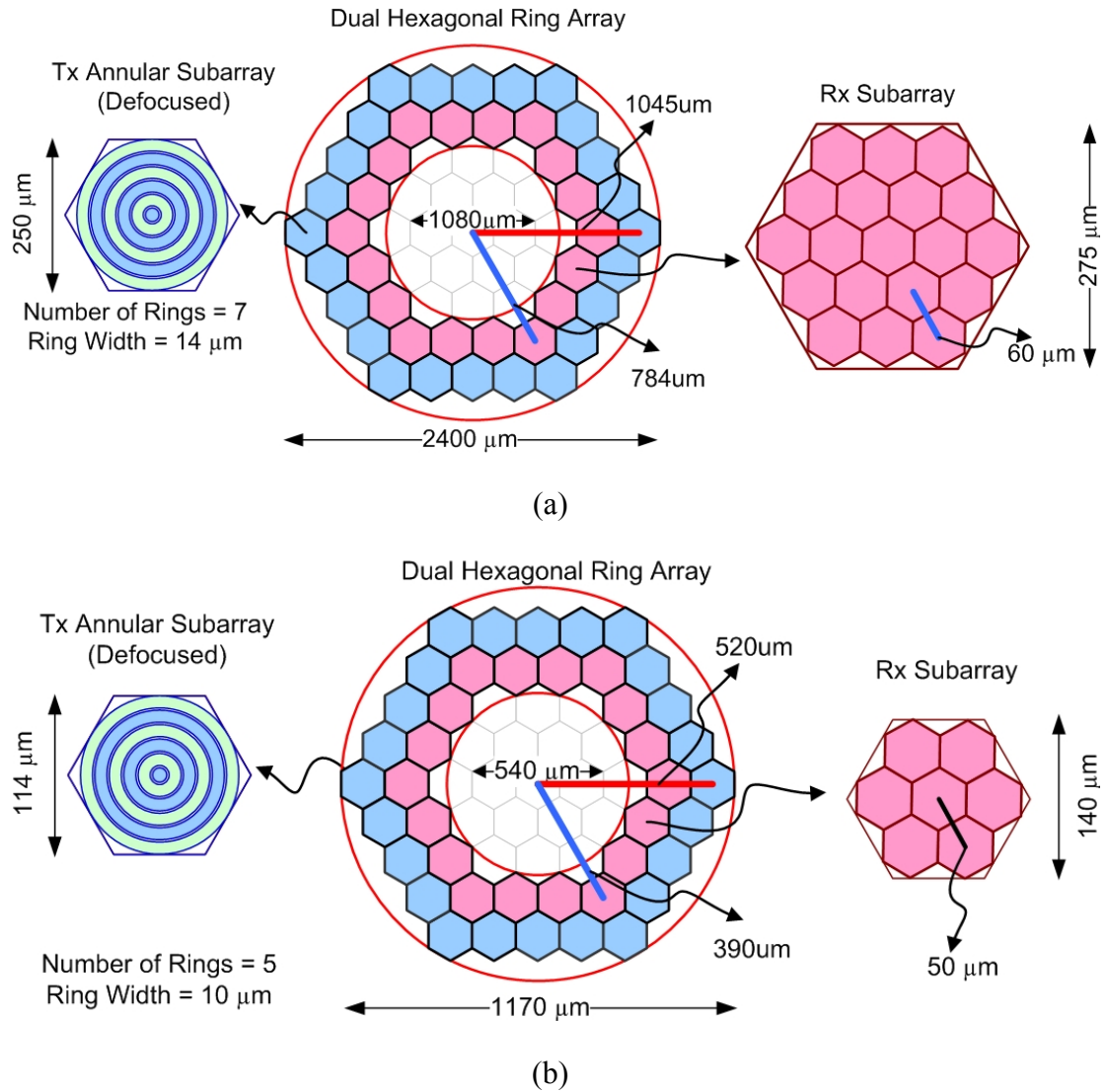
Figure 7.4. Schematic description of dual hexagonal array structures for (a) ICE and (b) IVUS configurations.

Full Hexagon Array
(Phased Array)

Dual Hexagonal Ring Array
(Phased Array)

Dual Hexagonal Ring Array
With Non-redundant Coarray
(Synthetic Phased Array)

PSF of target (f/4) on $\theta\phi$–surface ($0\leq\phi\leq2\pi$, $0\leq\theta\leq\pi/2$)

PSF of target (f/4) on $\rho\phi$–surface

Figure 7.5. 2-D PSFs of Full hexagonal, dual hexagonal and dual hexagonal with non-redundant coarray.

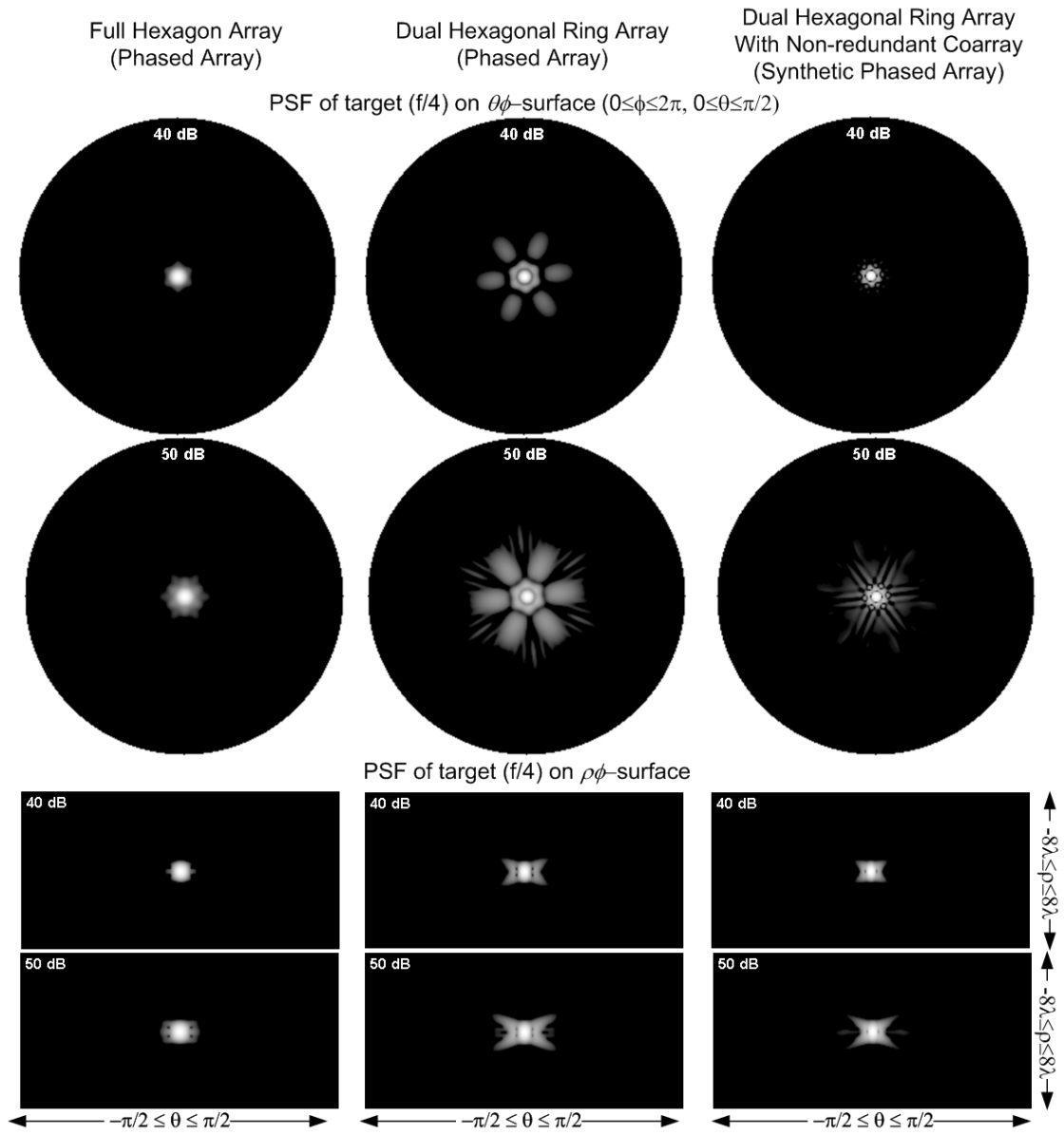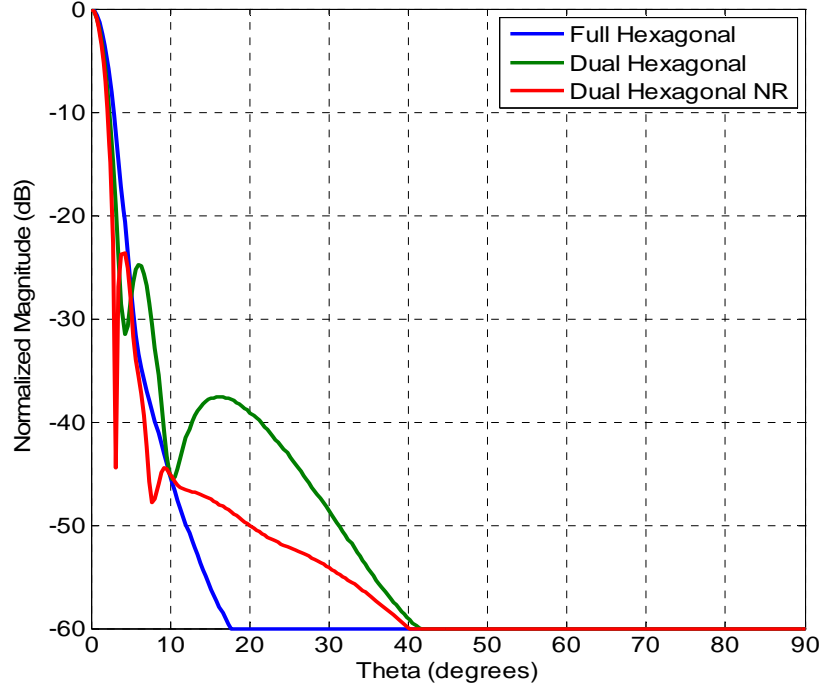Figure 7.6. 1-D PSFs of Full hexagonal, dual hexagonal and dual hexagonal with non-redundant coarray.

For the PSF simulations of dual hexagonal ring array of ICE configuration we used a gaussian pulse with a center frequency of 10 Mhz. The speed of sound is equal to 1540 m/s and the sampling frequency is 2 GHz. The fractional bandwidth is chosen as 50% . For displaying 2-D PSFs, we used constant-r surface ($\theta\varphi$-surface) and $r\theta$-plane (in spherical coordinates as depicted Figure 6.3), which correspond to the C-scan and B-scan displays, respectively. Each image in these figures was normalized to its own maximum and log compressed to 40 dB and 50 dB dynamic range. Here the target is located on the array normal (on axis) at $f/4$, and hence these PSFs represent non-steered beam patterns. The C-scan and B-scan images are shown in Figure 7.5 (top, bottom). For ease of comparison, we also obtained averaged 1-D lateral cross-sections of the PSFs shown in Figure 7.6, where the averaging was performed by the 1-D cross-sections across the entire φ-range and the r-range, respectively.

When we examine the PSF results, we observe that the three cases have identical main lobe performances. For the peak near side lobe level the dual hexagon non-

redundant coarray case, as expected, has better performance than the full Tx-Rx dual hexagon case.

7.4. Optimization

We performed simulated annealing optimization technique to reduce the number of firings in dual hexagonal array. The optimization results are obtained for 516 and 258 element cases, whereas the full set has 1176 elements with eliminated redundancy.

For the simulation parameters we used: 400 iterations, 2000 perturbations and the initial temperature value of 2 to obtain the optimized set. The temperature function with a parameter 0.97 is used in Equation 6.7. We performed the simulations by selecting the proper energy function that minimizes the peak side lobe. To obtain a circularly symmetric coarray as well as PSF distribution and reduce the search space as well as the computational time we choose the elements from one sixth of the coarray space and extend the solution by using symmetricity. This also results in symmetric Tx-Rx firing pairs. The coarrays produced by all the Tx-Rx element pairs (fullset), 516-element and 258-element and optimized cases with their corresponding B-scans and C-scans are shown in Figure 7.7.

For an easier comparison of the PSF performances we also plot averaged 1-D cross-sectional PSFs. The optimized array configurations produce considerably better performance than the full set, however their -6 dB main lobe widths are wider. This is because of extremely sparse structure of the outer elements for the optimized coarray. However, the full set have equal inter-element distance on the whole coarray space. For the two optimized cases, the far side lobes and/or grating lobes remain under -40dB over the angle of 45°. The simulation results showed that simulated annealing algorithm produce satisfactory results on the optimization of dual hexagon arrays.
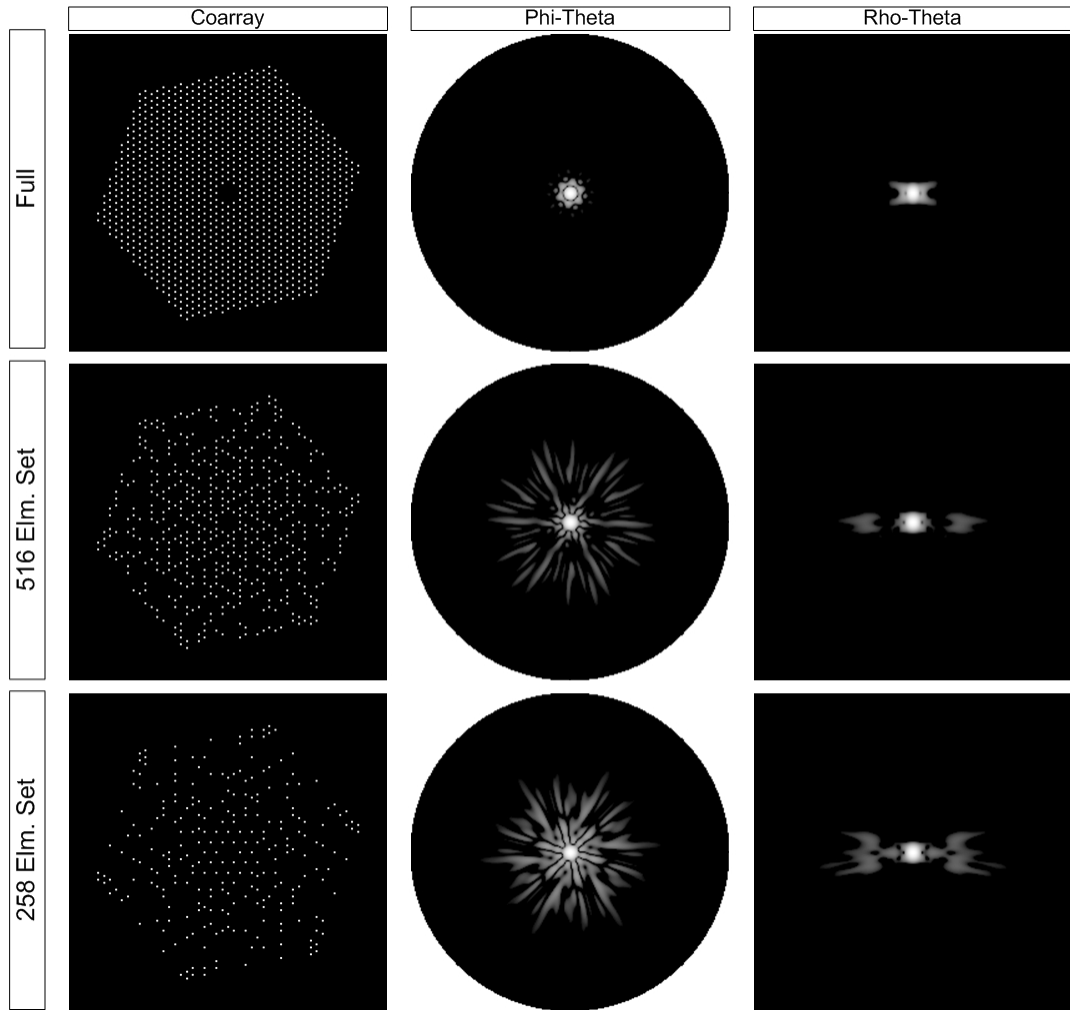
Figure 7.7. Coarray and PSF images of full and optimized reduced sets for dual hexagon arrays.
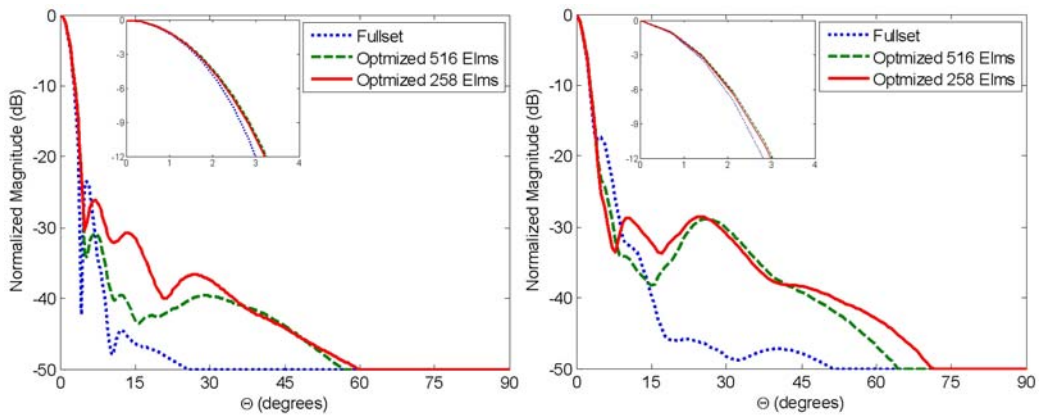

Figure 7.8. 1-D PSFs full and optimized reduced sets for dual hexagon arrays (left) in constant-r and constant-φ surfaces (right).

Chapter 8
Conclusion

In this dissertation, we proposed and examined two different array architectures suitable for FL-IVUS and ICE imaging. Forward looking catheters have volumetric imaging capability which is highly desirable in IVUS and ICE applications. A ring shaped array configuration is especially suitable for FL-IVUS since a guide wire is required in catheters. The CMUT technology is promising for FL-IVUS imaging since it offers high bandwidth, good sensitivity and flexibility to fabricate arrays of different shapes and sizes. In addition, it enables monolithic or flip-chip-bonding-based electronics integration. By taking advantage of the flexibility offered by CMUT technology, it is possible to utilize the area around the guide wire efficiently by implementing multiple-ring arrays for FL-IVUS imaging.

FL-IVUS imaging system needs to be small due to limited sizes on the front tip of IVUS catheters. This leaves a very small area for the array elements and front-end electronics. One of the main challenges in the array based FL-IVUS systems is the large channel count which results in increased system complexity. Synthetic phased array processing with reduced firing count simplifies the front-end and hence can enable 3-D real-time imaging. For the need to reduce the number of channels and/or firing count, an optimization procedure has to be developed. The main objective of the optimization should be to discover a suitable array/firing configuration with an optimal image quality.

This study is mainly focused on designing new array architectures and developing array processing techniques to optimize image quality while reducing firing events which enables real time 3-D volumetric imaging. For this purpose, we proposed two array designs which are dual circular ring and dual hexagonal ring array. Both array designs are in ring-shaped structure and composed of independent transmit and receive arrays which simplifies the front-end electronics.

Features and optimization procedures for dual ring array were investigated in detail and compared the results with the single ring arrays. For the optimization of image quality, we used coarray concept with different sampling schemes. Due to its cumbersome geometry we used a powerful optimization algorithm called simulated annealing to find optimal solutions. Comparable wide-band analysis are obtained and presented to show the feasibility of the procedures.

The hexagonal ring array structure together with formation of the structure and two different array configurations were presented. Besides the advantage of increasing SNR, the dual hexagonal array structure produces reasonable image performance in FL-IVUS and ICE imaging. The simulated annealing algorithm is also performed for dual hexagon arrays and the results are presented.

The proposed designs and used array processing techniques give satisfactory results to overcome the challenges in catheter based forward looking ultrasound imaging applications. For future work, the presented work and obtained results can be verified by the experimental studies. This may results some new approaches based on the presented work.

Bibliography

[1] Awad, S., *Lesion Enhancement for Three Dimensional Rectilinear Ultrasound Imaging*, Ph. D. Dissertation, University of Southern California, 2009.

[2] Sethuraman, S., *Combined Intravascular Ultrasound and Photoacoustic Imaging*, Ph. D. Dissertation, University of Texas, 2007.

[3] De Korte, C., Van Der Steen, A., Cespedes, E. and Pasterkamp, G., "Intravascular Ultrasound Elastography in Human Arteries: Initial Experience 118 In Vitro", *Ultrasound In Medicine and Biology,* vol. 24, pp. 401-408, 1998.

[4] Doyley, M., Mastik, F., De Korte, C., Carlier, S., Cespedes, E., Serruys, P., Bom, N. and Van Der Steen, A., "Advancing Intravascular Ultrasonic Palpation Toward Clinical Applications", *Ultrasound In Medicine and Biology,* vol. 27, pp. 1471-1480, 2001.

[5] Kimura, B., Bhargava, V. and Demaria, A., "Value and Limitations Sf Intravascular Ultrasound Imaging in Characterizing Coronary Atherosclerotic Plaque", *American Heart Journal,* vol. 130, pp. 386-396, Aug 1995.

[6] Stephens, D. N., *et al.*, "Forward Looking Intracardiac Imaging Catheters for Electrophysiology", *IEEE Ultrasonics Symposium,* 2006.

[7] Nikoozadeh, A., *et al.*, "Forward-Looking Intracardiac Ultrasound Imaging Using a 1-D CMUT Array Integrated With Custom Front-End Electronic", *IEEE Trans Ultrason Ferroelectr Freq Control,* vol. 55, no. 12, 2008.

[8] Courtney, B. K., *et al.*, "Innovations in Imaging for Chronic Total Occlusions: a Glimpse into The Future of Angiography's Blind-spot", *Eur Heart J,* **29**(5), 583-93., 2008.

[9] Cuneo, A. and Tebbe, U., "The Management of Chronic Total Coronary Occlusions" *Minerva Cardioangiol,* **56**(5), 527-41., 2008.

[10] Van Der Steen A., *et al.*, "IVUS Beyond The Horizon", *Euro Intervention,* **2**(5), 132-142., 2006.

[11] Ng, K., *et al.*, "Arterial Imaging with a New Forward-Viewing Intravascular Ultrasound Catheter, II. Three-dimensional Reconstruction and Display of Data", *Circulation,* **89**(2), 718-723., 1994.

[12] Van Der Steen, A. and Saijo, Y., *Vascular Ultrasound*, Springer-Verlag, Tokyo, Japan, 2003.

[13] Wang, Y., Stephens, D. N. and O'Donnell, M., "A Forward Viewing Ring-Annular Ultrasound Array for Intravascular Imaging," *Proc. IEEE Ultrason. Symp.*, pp. 1573–1576, 2001.

[14] Yao, W., Stephens, D. N. and O'Donnell, M., "A Forward-Viewing Ring-Annular Array for Intravascular Ultrasound Imaging", *IEEE Ultrasonics Symposium,* 2001.

[15] Yeh, D.T., *et al.*, "3-D Ultrasound Imaging Using a Forward-Looking CMUT Ring Array for Intravascular/Intracardiac Applications", *IEEE Trans Ultrason Ferr. Freq Control,* **53**(6), pp. 1202-1211., 2006.

[16] Degertekin, F. L., Guldiken, R. O. and Karaman, M., "Annular-Ring CMUT Arrays for Forward-Looking IVUS: Transducer Characterization and Imaging", *IEEE Trans Ultrason Ferroelectr Freq Control,* **53**(2), pp. 474-82, 2006.

[17] Smith, S. W., Pavey, H. G. and von Ramm, O. T., "High Speed Ultrasound Volumetric Imaging System-Part I: Transducer Design and Beam Steering," *IEEE Trans. Ultrason., Ferroelect., Freq. Contr.,* vol.38, pp.100-108, 1991.

[18] Lockwood, G. R. and Foster, F. S., "Optimizing The Radiation Pattern of Sparse Periodic Two-Dimensional Arrays," *IEEE Trans. Ultrason., Ferroelect., Freq. Contr.*, vol. 43, no. 1, pp. 15–19, 1996.

[19] Austeng, A., Holm, S., Weber, P.K., Aakvaag, N., Iranpour, K., "1D and 2D Algorithmically Optimized Sparse Arrays", *Proc. IEEE Ultrason. Symp.*, vol. 2, pp. 1683–1686, Toronto, Canada, 1997.

[20] Holm, S., Elgetun, B. and Dahl, G., "Properties of The Beampattern of Weight- and Layout-Optimized Sparse Array", *IEEE Trans. Ultrason., Ferroelect., Req. Contr.,* vol. 44, no. 5, pp. 983-991, 1997.

[21] Holm, S., Elgetun, B. and Dahl G., "Weight- and Layout-Optimized Sparse Arrays", *Proc. Int. Workshop on Sampling Theory Appl.,* pp. 97-102, 1997.

[22] Holm, S., Elgetun, B. and Dahl, G., "Properties of The Beampattern of Weight- and Layout-Optimized Sparse Array", *IEEE Trans. Ultrason., Ferroelect., Req. Contr.,* vol. 44, no. 5, pp. 983-991, 1997.

[23] Trucco, A., "Thinning and Weighting of Large Planar Arrays by Simulated Annealing", *IEEE Trans. Ultrason., Ferroelect., Freq. Contr.,* **46**(2), pp. 347–355, 1997.

[24] Caorsi, S., Trucco, A., "Planar Antenna Array Design with a Multi-Purpose GA-Based Procedure", *Microwave and Optical Technology Letters,* Vol. 35, No. 6, 2002.

[25] Angelsen, B. A. J., *Waves, Signals and Signal Processing in Medical Ultrasonics,* Department of Physiology and Biomedical Engineering, Norwegian University of Science and Technology, 1996.

[26] Goodman, J. W., *Introduction to Fourier Optics*. McGraw Hill, Boston, 1968.

[27] Johnson, J. A., *Coherent Array Imaging Using Phased Subarrays*, Ph. D. Dissertation, Stanford University, 2003.

[28] Shoup, T. A. and Hart, J., "Ultrasonic Imaging Systems", *Proc. IEEE Ultrasonics Symp.,* pp. 863-871, 1998.

[29] Karaman, M., Li, P. C., and O'Donnell, M., "Synthetic Aperture Imaging for Small Scale Systems", *IEEE Trans. Ultrason., Ferroelect., Freq. Contr.,* vol. 42, pp. 429-442, 1995.

[30] Karaman, M. and O'Donnell, M., "Subaperture Processing for Ultrasonic Imaging", *IEEE Trans. Ultrason., Ferroelect. Freq. Contr.,* vol. 45, pp. 429-442, 1998.

[31] Oralkan, O., *Acoustical Imaging Using Capacitive Micromachined Uultrasonic Transducer,* Ph. D. Dissertation, Stanford Universty, 2004.

[32] Yao, H., *Synthetic Aperture Methods for Medical Ultrasonic Imaging,* M. Sc. Thesis, University of Oslo, 1997.

[33] Khuri-Yakub, B. T., *http:/www.kyg.stanford.edu/khuriyakub/opencms/en /research /cmuts /general/index.html*

[34] Kino, G. S., *Acoustic Waves: Devices, Imaging, and Analog Signal Processing.*

[35] Cook, W. J., Cunningham, W. H., Pulleyblank, W. R., Schrijver, A., *Combinatorial Optimization*, John Wiley & Sons, 1998.

[36] Kirkpatrick, S., Gelatt Jr., C. D., Vecchi, M. P., "Optimization by Simulated Annealing", *Science*, vol. 220, no. 4598, 1983.

[37] Murino, V., Trucco, A., Regazzoni, C. S., "Synthesis of Unequally Spaced Arrays by Simulated Annealing", *IEEE Transactions on Signal Processing*, vol. 44, no. 1, 1996.

[38] Trucco, A., Repetto, F., "A Stochastic Approach to Optimizing the Aperture and the Number of Elements of an Aperiodic Array", *Oceans96*, pp. 1510-1515, 1996.

[39] van Laarhoven, P. J. M., Aarts, E. H. L., "Simulated Annealing: Theory and Applications", *D. Reidel Publishing Company*, 1987.

[40] Aarts, E., Lenstra, J. K., *Local Search in Combinatorial Optimization,* Wiley-Interscience series in discrete mathematics and optimization, 1997.

[41] Wang, Y., Stephens, D. N. and O'Donnell, M., "Optimizing The Beam Pattern of a Forward-Viewing Ring-Annular Ultrasound Array for Intravascular Imaging", *IEEE Transactions on Ultrasonics, Ferroelectrics and Frequency Control,***49**(12), pp. 1652-1664, 2002.

[42] Yeh, D. T., *et al.*, "3-D Ultrasound Imaging Using A Forward-Looking CMUT Ring Array for Intravascular/Intracardiac Applications", *IEEE Trans Ultrason Ferroelectr Freq Control,* **53**(6), pp. 1202-11, 2006

[43] von Ramm, O. T. and Smith, S. W., "Beam Steering with Linear Arrays", *IEEE Trans. Biomed. Eng.*, vol. BME-30, no. 8, pp. 438-452, 1983.

[44] Thomenius, K. E., "Evolution of Ultrasound Beamformers", *Proc. IEEE Ultrasonics Symp.*, pp. 1615-1622, 1996.

[45] Steinberg, B. D., *Principles of Aperture and Array System Design: Including Random and Adaptive Arrays.*, John Wiley & Sons, New York, 1976.

[46] Turnbull, D. H. and Foster, F. S., "Beam Steering with Pulsed Two-Dimensional Transducer Arrays", *IEEE Trans. Ultrason., Ferroelect., Freq. Cont.*, vol. 38, pp. 320-333, 1991.

[47] Selfridge, A. R., Kino, G. S. and Khuri-Yakub, B. T., "A Theory for The Radiation Pattern of A Narrow Strip Acoustic Transducer", *Appl. Phy. Lett.*, vol. 37, no. 1, pp. 35-36, 1980.

[48] Johnson, J. A., Karaman, M., Khuri-Yakub, B. T., "Synthetic Phased Array Image Formation and Restoration", *Proc. IEEE Int. Conf. on Acoustics, Speech and Signal Processing*, pp. 2885-2887, 2002.

[49] Norton, S. J., "Annular Array Imaging with Full-Aperture Resolution", *J.Acoust. Soc. Am.*, vol. 92, pp. 3202-3206, 1992.

[50] Guldiken, R., *et al.*, "Forward-Looking IVUS Imaging Using a Dual-Annular Ring CMUT Array: Experimental Results", *IEEE Ultrasonics Symposium,* 2007.

[51] Crowe, J. R., Hamilton, J. D., Stephens, D. N., Wang, Y. and O'Donnell, M., "Modified Weighting Method for Forward-Looking Ring-Annular Arrays", *IEEE Ultrason. Imag.*, vol. 23, pp. 19–38, 2001.

[52] Degertekin, F. L., Guldiken, R. O. and Karaman, M., "Annular-Ring CMUT Arrays for Forward-Looking IVUS: Transducer Characterization and Imaging", *IEEE Trans Ultrason Ferroelectr Freq Control,* **53**(2), pp. 474-82, 2006.

[53] Tekes, C., Karaman, M., Degertekin, F. L., "Co-array Optimization of CMUT Arrays for Forward-Looking IVUS", *IEEE Ultrasonics Symposium,* Rome, 2009.

[54] Guldiken, R., Zahorian, J., Balantekin, M., Degertekin, F. L., Tekes, C., Sisman, A., Karaman, M., "Dual-Annular-Ring CMUT Array for Forward Looking IVUS Imaging", *IEEE Ultrasonics Symposium,* pp. 698 – 701, 2006.

[55] Tekeş, C., Karaman, M., "Ultrasonik Görüntülemede Eşdeğer Dizi Eniyilenmesi", *Biyomedikal Mühendisliği Ulusal Toplantısı (BİYOMUT),* İstanbul, 2007.

[56] Tekeş, C., Karaman, M., "Damar İçi Öne Bakan Ultrasonik Görüntüleme için Eşdeğer Dizi Örnekleme Yöntemleri", *Biyomedikal Mühendisliği Ulusal Toplantısı (BİYOMUT),* İzmir, 2009.

Curriculum Vitae

Coşkun Tekeş was born on 14 February 1976, in İstanbul. He attended İstanbul Technical University and received his BS degree in Electrical Engineering in 1998. He received M.S. degree in Electronics Engineering from Işık Universliy in 2002. During his master education he worked as an R&D engineer in private company. He continued his business carrier in Mobiarts Communication Services for 5 years as a co-founder and technical director. He has started his PhD education in Işık University in 2002. He also worked as a research assistant at the department of electronics engineering of Işık University since 2003. He worked on medical ultrasound imaging and array processing techniques during his PhD education. He has 10 years experience on industrial electronics, microcontroller based system design, data transfer over wireless networks and GPS based vehicle tracking systems.

Publications:

[1]   Tekes, C., Karaman, M., Degertekin, F. L., "Circular Ring Array Optimization for Forward-Looking IVUS Imaging", (in preperation).

[2]   Guldiken, R. O., Zahorian, J., Gurun, G., Balantekin, M., Degertekin, F. L., Tekes, C., Karaman, M., Qureshi, M. S., Hasler, P. "Microfabrication and Testing of a Dual-Ring CMUT Array for Forward Looking IVUS Imaging", (Revised and to be resubmited).

[3]   Tekes, C., Karaman, M., Degertekin, F. L., "Co-array Optimization of CMUT Arrays for Forward-Looking IVUS", *IEEE Ultrasonics Symposium,* Rome, 2009.

[4]   Tekeş, C., Karaman, M., "Damar İçi Öne Bakan Ultrasonik Görüntüleme için Eşdeğer Dizi Örnekleme Yöntemleri", *Biyomedikal Mühendisliği Ulusal Toplantısı (BİYOMUT),* İzmir, 2009.

[5]   Tekeş, C., Karaman, M., "Ultrasonik Görüntülemede Eşdeğer Dizi Eniyilenmesi", *Biyomedikal Mühendisliği Ulusal Toplantısı (BİYOMUT),* İstanbul, 2007.

[6]   Guldiken, R., Zahorian, J., Gurun, G., Qureshi, S., Balantekin, M., Tekeş, C., Hasler, P., Karaman, M., Carlier, S., Degertekin, F. L., "Forward-Looking IVUS Imaging Using a Dual-Annular Ring CMUT Array: Experimental Results", *IEEE Ultrasonics Symposium,* pp. 1247-1250, New York, 2007.

[7]   Guldiken, R., Zahorian, J., Balantekin, M., Degertekin, F.L., Tekes, C., Sisman, A., Karaman, M. "Dual-Annular-Ring CMUT Array for Forward Looking IVUS Imaging", *IEEE Ultrasonics Symposium*, pp.698 − 701, 2006.